Year-long, broad-band, microwave backscatter observations of an Alpine Meadow over the Tibetan Plateau with a ground-based scatterometer

Jan G. Hofste[1], Rogier van der Velde[1], Jun Wen[2], Xin Wang[3], Zuoliang Wang[3], Donghai Zheng[4], Christiaan van der Tol[1], and Zhongbo Su[1]

[1]Faculty of Geo-Information Science and Earth Observation (ITC), University of Twente, Enschede, Netherlands
[2]College of Atmospheric Sciences, Plateau Atmosphere and Environment Key Laboratory of Sichuan Province, Chengdu University of Information Technology, Chengdu, China
[3]Key laboratory of Land Surface Process and Climate Change in Cold and Arid Regions, Northwest Institute of Eco-Environment and Resources, Chinese Academy of Sciences, Lanzhou, China
[4]National Tibetan Plateau Data Center, Institute of Tibetan Plateau Research, Chinese Academy of Sciences, Beijing, China

Correspondence: Jan Hofste (j.g.hofste@utwente.nl)

Abstract. A ground-based scatterometer was installed on an alpine meadow over the Tibetan Plateau to study the soil moisture and -temperature dynamics of the top soil layer and air–soil interface during the period August 2017 – August 2018. The deployed system measured the amplitude and phase of the ground surface radar return at hourly and half-hourly intervals over $1 - 10$ GHz in the four linear polarization combinations (vv, hh, hv, vh). In this paper we describe the developed scatterometer system, gathered datasets, retrieval method for the backscattering coefficient (σ^0), and results of σ^0 ~~for co-polarization~~.

The system was installed on a 5 m high tower and designed using only commercially available components: a Vector Network Analyser (VNA), four coaxial cables, and two dual polarization broadband gain horn antennas at a fixed position and orientation. We provide a detailed description on how to retrieve the ~~co-polarized backscattering coefficients σ_{vv}^0 & σ_{hh}^0 for~~ backscattering coefficients for all four linear polarization combinations σ_{pq}^0, where p is the received- and q the transmitted polarization (v or h), for this specific scatterometer design. To account for the particular effects caused by wide antenna radiation patterns (G) at lower frequencies, σ^0 was calculated using the narrow-beam approximation combined with a mapping of the function G^2/R^4 over the ground surface. (R is the distance between antennas and the infinitesimal patches of ground surface.) This approach allowed for a proper derivation of footprint positions and -areas, and incidence angle ranges. The frequency averaging technique was used to reduce the effects of fading on the ~~σ^0~~ σ_{pq}^0 uncertainty. Absolute calibration of the scatterometer was achieved with ~~measured backscatter from~~ measurements of a rectangular metal plate ~~as reference target~~ and rotated dihedral metal reflectors as reference targets.

In the retrieved time-series of ~~σ_{vv}^0 & σ_{hh}^0 for~~ σ_{pq}^0 for L-band ($1.5 - 1.75$ GHz), S-band ($2.5 - 3.0$ GHz), C-band ($4.5 - 5.0$ GHz), and X-band ($9.0 - 10.0$ GHz) we observed characteristic changes or features that can be attributed to seasonal or diurnal changes in the soil~~. For~~: for example a fully frozen top soil, diurnal freeze-thaw changes in the top soil, emerging vegetation

in spring, and drying of soil. Our preliminary analysis ~~on the collected σ^0~~ of the collected σ_{pq}^0 time-series data set demonstrates that it contains valuable information on water- and energy exchange directly below the air-soil interface~~. Information~~, information which is difficult to quantify, at that particular position, with in-situ measurements techniques alone.

Availability of backscattering data for multiple frequency bands (raw radar return and retrieved σ_{pq}^0) allows for studying scattering effects at different depths within the soil and vegetation canopy during the spring and summer periods. Hence further investigation of this scatterometer data set provides an opportunity to gain new insights in hydro-meteorological processes, such as freezing and thawing, and how these can be monitored with multi-frequency scatterometer observations. The data set

30 is available via https://~~doi.org~~doi-org.ezproxy2.utwente.nl/10.17026/~~dans-ze5-skyg (?)~~dans-zfb-qegy (?). Software code for processing the data and retrieving σ_{pq}^0 via the method presented in this paper can be found under https://doi-org.ezproxy2.utwente.nl/10.1702 (?)

~~The effects of fading, calibration, and system stability on the uncertainty in σ^0 are estimated to vary from ± 1.3 for X-band~~
35 ~~with vv-polarization to ± 2.7 for S-band with hh-polarization through the campaign. The low angular resolution of the antennas~~ ~~result in additional σ^0 uncertainty, one that is more difficult to quantify.Estimations point out that it probably will not exceed~~ ~~± 2 with C-band.Despite these uncertainties, we believe that the strength of our approach lies in the capability of measuring~~ ~~σ^0 dynamics over a broad frequency range, $1-10$, with high temporal resolution over a full-year period.~~

Copyright statement. TEXT

40 # 1 Introduction

~~For accurate climate modelling~~ To comprehend the climate of the Tibetan Plateau, also known as the '~~third pole environment~~Third Pole Environment', the transfer processes of energy and water at the land-atmosphere interface must be understood ~~(?), (?)~~ ~~. Main quantities~~ (??). Main states of interest are the dynamics of soil moisture and -temperature (?). Together with sensors embedded into the deeper soil layers, microwave remote sensing is suitable to study these dynamics since it directly probes the
45 top soil layer within the antenna footprint.

A ground-based microwave observatory was installed on an alpine meadow over the Tibetan plateau, near the town of Maqu~~(China)~~. The observatory consists of a ~~(passive)~~ microwave radiometer system called ELBARA-III (ETH L-Band radiometer for soil moisture research) ~~(?), (?), and an (active)~~ (??), and an microwave scatterometer. Both continuously measure
50 the surface's microwave signatures with a temporal frequency of once every hour~~year round~~. The ELBARA-III was installed in January 2016 and is currently still measuring ~~(?)~~(??), the scatterometer was installed in August 2017 and continued to operate

until July 2019.

This paper describes the scatterometer system and the ~~dataset that has been collected~~ collected dataset over the period August 2017 – August 2018 ~~(?). The scatterometer was built with commercially available components: a vector network analyser (VNA), four phase stable coaxial cables, two dual polarization broadband gain horn antennas, and a laptop controlling the scatterometer's operation autonomously. The~~ (?). The radar return amplitude and phase were measured over a broad 1- 10 GHz frequency band at all four linear polarization combinations (vv, hv, vh, hh). ~~In this paper the co-polarizations results shall be discussed.~~ The scatterometer measured the radar return over a prolonged ~~time~~ period with its antennas in a fixed ~~position and~~ orientation, resulting in frequency-dependent incidence angle ranges varying from of ~~$20° \leq \theta \leq 65°$~~ $0° \leq \theta \leq 60°$ for L-band (~~1.25~~ 1.625 GHz) to $47° \leq \theta \leq 59°$ for X-band (9.5 GHz). During the summers of 2017 and 2018 additional experiments were conducted to asses the angular dependence of the backscatter and homogeneity of the local ground surface.

Many other studies exist employing ground-based systems to study microwave backscatter from land. Rather than an airborne- or spaceborne system, ground-based systems allow for high temporal ~~resolution~~ coverage and a high degree of control over the experimental circumstances. **?** and **?** ~~use~~ used specially developed radar systems by ProSensing Inc. to study backscattering from sea ice in the period 2004 - 2011: one system for C- and another for X- & Ku-band. Details on a similar ~~system for~~ S-band system can be found in **?**. The SnowScat system, developed by Gamma Remote Sensing AG (**?**), is another ~~specifically designed~~ scatterometer that operates over 9 - 18 GHz and measures the full polarimetric backscatter autonomously over many elevation- and azimuth angles. ~~SnowScat was used~~ **?** used it during multiple winter campaigns in the 2009 - 2012 period at two different locations to study the scattering properties of snow layers~~(?)~~. Like in this study, others also designed their scatterometer architecture around a commercially available ~~VNA~~ vector network analyser (VNA). For instance, ~~(?)~~ **?** used data measured by a truck-based system, operating at C- and L-band, in ~~the 2002 summer~~ summer 2002 to study the influence of corn on the retrieval of soil moisture from microwave backscattering. For every band they placed one antenna for transmit and receive on top of a boom. Selection of the individual polarization channels was realized using ~~RF~~ radio-frequency switches. Similar is the University of Florida L-band Automatic Radar System (UF-LARS) (**?**), used by, for example **?**, to measure soil moisture at L-band from a Genie-platform during ~~the 2012 summer .~~ summer 2012. Another example is the Hongik Polarimetric Scatterometer (HPS) (**?**), with which microwave backscatter from bean- and corn fields was measured in 2010 and 2013 respectively (**?**). Similar to our study, **?** used a scatterometer with its antenna in a fixed position and orientation to measure the backscattering during all growth stages of winter wheat at L-, C- and X-band during 2011 - 2012.

The temporal resolution and measurement period covered by the scatterometer data set reported in this paper permits studying both seasonal- and diurnal dynamics of microwave backscattering from an Alpine meadow ecosystem. This in turn allows for investigating the local soil moisture ~~content~~ dynamics, the freeze-thaw process, and growth/decay stages of vegetation. Because of the broad frequency range measured (1 – 10 GHz), wavelength-dependent effects of surface roughness and vegetation

scattering can be studied as well.

This paper is organized as follows. First ~~, details on the measurement site and present instruments are given. Followed by details on~~ the ~~scatterometer instrumentation, -setup, -geometries, and -calibration, along with a description of all performed experiments. Next the calculation method for~~ study area is described. Next, details are provided on the used instrumentation, performed measurements, and method for retrieving the backscattering coefficient ~~, or normalized radar cross section,~~ σ^0 ~~is described. Given the system's configuration we show what assumptions and approximation were made for calculating~~ $(\mathrm{m^2\,m^{-2}})$. We then present an overview of the retrieved σ^0 ~~from the measured radar return amplitude- and phase data. We then show some measurement results of~~ time series dataset and show how σ^0 ~~. These are the angular response of σ^0 for asphalt, experiments to explore the angular~~ varies across seasons and on a diurnal timescale. In the discussion section the ~~angular-~~ and spatial variability of σ^0 at the ~~measurement site, and finally some results of the time-series of~~ study area and measurement uncertainty are described. Technical details on all aspects of the scatterometer measurements and σ^0 calculation are included in the annex. A list of ~~used~~ symbols can be found at the end of this paper.

2 ~~Measurement site~~ Study region and climate

2.1 ~~Maqu site~~

In August 2017 the scatterometer was installed on the tower of the Maqu measurement site (Maqu site) (**?**), and operated over the period August 2017 – June 2019. The Maqu site is situated in an Alpine meadow ecosystem (**?**) on the Tibetan plateau~~.,~~ Fig. 1(a). The site's coordinates are $33°55'$ N, $102°10'$ E, at $3500\,\mathrm{m}$ elevation. The site is located close to the town Maqu of the Gansu province of China.

Besides the scatterometer, other remote sensing sensors placed on the tower are the ELBARA-III radiometer (**?**) and the optical spectroradiometer system 'Piccolo' (**?**), ~~see Fig.??~~ Fig.1(b). The ELBARA-III system has been measuring L-band microwave emission from January 2016 to this date ~~(?)~~(**??**). The Piccolo system measured the reflectance and sun-induced chlorophyll fluorescence of the vegetation over the period July - November 2018.

2.1 ~~Climate~~

According to **?** the climate at Maqu is characterized by the Köppen-Geiger classification as '~~Dw~~Dwb', Cold with dry winters. Winter (December - February) and spring (March - May) are cold and dry while the summer (June - August) and autumn (August - November) are mild with monsoon rain.~~Over 2018, during the coldest period in January the diurnal air temperature varied from -24 to -3 while in summer, during the warmest period in August the diurnal air temperature varied from 8 to 18 . The top soil temperature drops below 0 in- and around the winter period, while from mid spring to mid autumn soil temperature at all depths remain above this temperature. Measurements with the thermistors of the 5TM sensor array showed that during~~
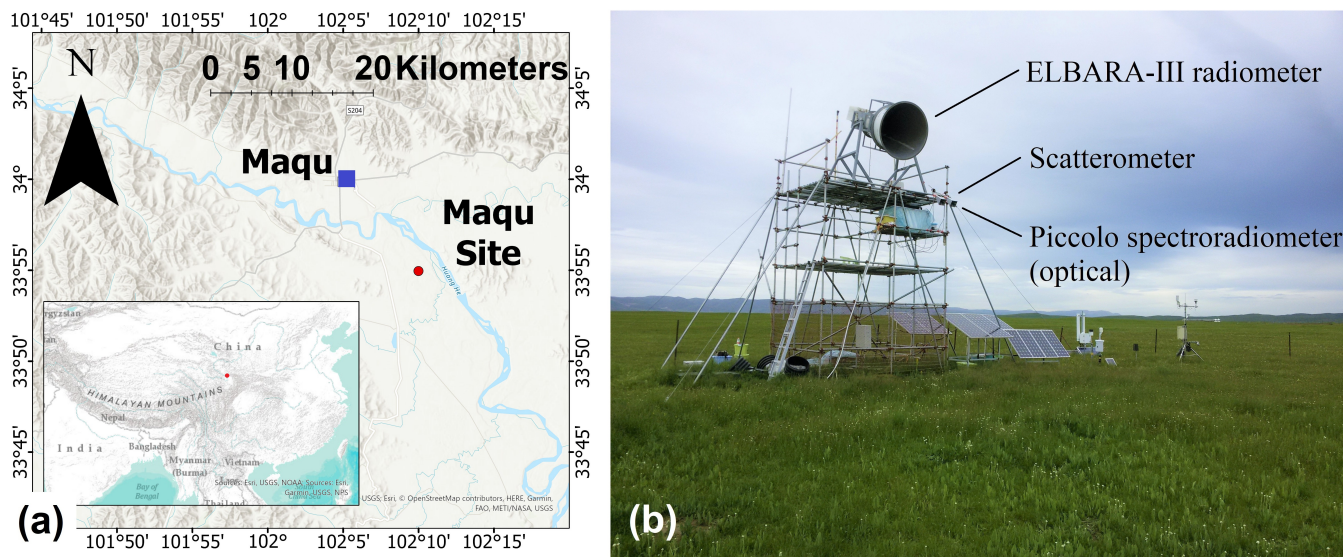
Figure 1. (a) Location of Maqu measurement site on eastern part of the Tibetan Plateau. (b) Tower of Maqu site containing the scatterometer, the ELBARA-III radiometer, and Piccolo optical spectroradiometer.

the 2018 winter the soil temperature dropped below 0 up to a depth of 70 . From August 2017 to July 2018 the precipitation per season was: 419 in autumn, 2 in winter, 41 in spring, and 128 in summer.

2.1 ~~Vegetation~~

The ecosystem classification of the Maqu site is Alpine Meadow according to **?**. The vegetation around the Maqu site consists for a major part of grasses. The growing season starts at the end of April and ends in October, when above-ground biomass turns brown and loses its water. During the growing season the meadows are regularly grazed by lifestock. To prevent ~~this~~ the lifestock from entering the site and damaging the equipment a fence is placed around the Maqu site. As a result there is no grazing within the site, causing the vegetation to be more dense and higher than that of the surroundings. Also a layer of dead plant material from the previous year remains present below the newly emerged vegetation. In Appendix A1 some photographs are shown of the Maqu site during different seasons, which provide an impression of the site's phenology.

3 Methodology

3.1 Supporting Measurements

Together with the scatterometer measurements following hydrometeorological quantities were recorded over the period August 2017 – August 2018: depth profile of volumetric soil moisture m_v ($m^3\,m^{-3}$) and soil temperature T_{soil} (°C), air temperature T_{air} (°C), precipitation (mm), and the short- and long wave up- and downward irradiance ($W\,m^{-2}$). Details on used sensors can be found in Appendix A2.

135   The depth profile of m_v ($m^3\,m^{-3}$) was measured with an array of 20 capacitance sensors, type 5TM (manufacturer: Meter Group), that were installed at depths ranging from 2.5 cm to 1 m (**?**). All sensors in the array are also equipped with a thermistor, enabling the measurement of T_{soil} (°C). The soil moisture and -temperature was logged every 15 minutes for the period of August 2017 – August 2018 with Em50 data loggers (manufacturer: Meter Group) that were buried nearby the sensors. The location of the buried sensor array is indicated in Fig. 2. Results of these hydrometeorological measurements

140   over the period August 2017 – August 2018 can be found in Appendix A2 as well. With a hand-held impedance probe, type ThetaProbe ML2x (manufacturer: Delta-T Devices), the spatial variability of m_v in the top 2.5 – 5 cm soil layer over the Maqu site was measured (Appendix A3).

To quantify the vegetation cover at the Maqu site, ~~a set of~~ measurements were performed on two days during the 2018

145   summer~~:~~, namely 12 July and 17 August. Vegetation height, above-ground biomass (fresh & ~~over-dried~~oven-dried), and leaf area index (LAI) were measured at ten 1.2×1.2 m^2 sites around the periphery of the ~~no-step zone~~'No-step zone' indicated in Fig. 2. The ~~average quantities over the ten sites are summarized in Table A2. The~~ vegetation height of a single site was determined as the maximum value of the histogram obtained by taking ≥ 30 readings with a thin ruler at random points within the site area. For each site above-ground biomass and LAI were determined from harvested vegetation within one or two disk

150   areas defined by a 45 cm diameter ring. Immediately after harvest all biomass was placed in air-tight bags so that the fresh- and dry biomass could be determined by weighing the bag's content before and after ~~heating with~~drying in an oven. The LAI was determined immediately after harvest with part of the harvested fresh biomass by the ~~plotting~~ method described in **?**. ~~Measured vegetation parameters at Maqu-site during summer 2018 12 July 2018 17 August 2018 Height (distribution max.) () 25 40 Biomass Fresh () 0.9 1.3 Biomass Dry () 0.3 0.5 VWC () 60 62 LAI () 3.5 7 Map of the Maqu site. Scatterometer footprints for~~

155   ~~C-band with vv polarization shown for different incidence angles of antenna boresight line: $\alpha_0 = 40, 55, 70°$. Also shown are antenna azimuth angles ϕ.~~

3.2   ~~Hydrometeorological sensors~~

~~Table A1 lists all hydrometeorological instruments used for this study along with their reported measurement uncertainties. Air temperature was measured with a Platinum resistance thermometer, type HPM 45C, installed 1.5 m above the ground and~~

160   ~~precipitation (both rain and snow) was measured with a weight-based rain gauge, type T-200B~~The obtained average quantities over the ten sites are summarized in Appendix A4. ~~Overview of relevant Hydrometeorological sensors Maqu site Quantity Type, Manufacturer: Unit, Uncertainty: Volumetric soil moisture content m_v 5TM, Meter Group ± 0.02 (**?**)Volumetric soil moisture content m_v ThetaProbe ML2x, Delta-T Devices ± 0.05 Soil temperature 5TM, Meter Group ± 1 Air temperature HPM 45C, Campbell Scientific ± 1 Precipitation (rain & snow) T-200B, Geonor ± 0.6 The depth profile of volumetric soil~~

moisture content m_v () was measured with an array of 20 capacitance sensors, type 5TM, that were installed at depths ranging from 2.5 to 1 (?). All sensors in the array are also equipped with a thermistor, enabling the measurement of the soil temperature depth profile T_{soil} (). The soil moisture and -temperature was logged every 15 minutes for the period of August 2017 – August 2018 with Em50 data loggers (manufacturer: Meter Group) that were buried nearby with the sensors. The location of the buried sensor array is indicated in Fig. 2.

We estimate that the spatial average top soil moisture content over the Maqu site M_v () is linked to m_v as measured by the 5TM sensors at 2.5 and 5 depth (m_v^{5TM}) according to

$$M_v = m_v^{5TM} \pm S_{tot}$$

where S_{tot}, with value 0.04 , is the total standard deviation of spatially measured m_v with a hand held impedance probe, type ThetaProbe ML2x. Refer to Appendix ?? for additional information.

3.2 Scatterometer

4 Scatterometer and its operation

3.1 Instrumentation

3.0.1 Instrumentation

The main components of the scatterometer are a 2-port vector network analyser (VNA), type PNA-L 5232A (manufacturer: Keysight), four 3 m long phase stable coax cables, type Succoflex SF104PEA (manufacturer Huber + Suhner), and two dual polarization polarized broad band horn antennas, type BBHX9120LF (manufacturer: Schwarzbeck). The test port couplers of the VNA are removed and the coax cables are connected according to the schematic in , see Fig. B1. Connection scheme of scatterometer. Both dual polarization antennas, one for transmitting (TX) both polarizations and the other for receiving (RX) both polarizations, are connected to the VNA as indicated. Arrows indicate direction of signal. This configuration allows for measuring all four polarization channels: vv (transmit in vertical direction, receive in vertical direction), vh, vh, and hh. Between all four coaxial cables and their respective VNA connectors 10 attenuators, type SMA attenuator R411.810.121 (manufacturer: Radiall) were inserted to prevent interference from internal reflections travelling multiple times up- and down the coaxial cables. To protect the VNA from weather it is placed inside a water proof enclosure equipped with fans to provide air ventilation. The antenna radiation patterns are measured in the principal planes by the manufacturer over the 1 – 10 GHz band (?). As a summary, the full width half max maximum (FWHM) intensity beamwidths over frequency are shown in Appendix ??, Fig. B3. The scatterometer is placed on a tower as shown in Fig.??. The two antenna apertures are at a distance approximate $H_{ant} = 5$ above the ground (H_{ant} depends on the antenna boresight angle α_0) and are separated from each other horizontally by $W_{ant} = 0.4$. To protect the VNA from weather it is placed inside a water proof enclosure equipped with fans to provide air ventilation.

Deployed reference targets to calibrate the scatterometer ~~, and subsequently validate this calibration,~~ were a rectangular plate and two dihedral reflectors. The rectangular plate reflector was constructed from light-weight foam board covered with 100 μm aluminium foil and had frontal dimensions $a = 85$ cm $\times b = 65$ cm. A small dihedral reflector was constructed from steel, its frontal dimensions were $a = 57$ cm $\times b = 38$ cm. A second large dihedral reflector was also constructed with foam board and aluminium foil, its frontal dimensions were $a = 120$ cm $\times b = 65$ cm. A height-adjustable metal mast was used to position the reference targets. To minimize reflection from this mast it was covered by pyramidal absorbers, type 3640-300 (manufacturer: Holland Shielding), having a 35 dB reflection loss for normal incidence at 1 GHz~~under normal incidence.~~

3.1 Setup

~

Figure B2 shows all relevant geometries for the experiments performed.

3.0.1 Experimental Setup and -procedures

The scatterometer is placed on a tower as shown in Fig. 1(b). The two antenna apertures are at ~~distance H_{ant}~~ a distance approximate $H_{ant} = 5$ m above the ground ~~surface. The separation between the two antenna apertures $W_{ant} = 0.4$ is small compared to the target distance (ground or calibration standards) which justifies using the geometric centre of the two apertures for all calculations. Every area segment dA () of the ground surface has its own distance to the antennas R and angle of incidence θ. Angles α~~ H_{ant} depends on the antenna boresight angle α_0) ~~and β are angular coordinates of R. Angle α is defined between the tower's vertical axis and the orthogonal projection of the line from antennas to a ground surface segment onto the plane formed by the tower's vertical axis and the antenna boresight direction line. Angle β is defined between line from antennas to a ground surface segment and projection of that same line onto the plane formed by the tower's vertical axis and the antenna boresight direction line. The planes in which α and β lie are also the antenna's principal planes (see for example (?)). For the antenna boresight direction $\alpha = \alpha_0$ and $\beta = \beta_0$. The antenna rotation around the tower's vertical axis is defined as azimuth rotation ϕ.~~

~~Schematic of scatterometer geometry. (a) Every infinitesimal area dA has its own distance R to the geometric centre between antenna apertures (red dot) and angle of incidence θ. Angles α and β lie within the antennas principal planes, α_0 denotes the angle of antenna boresight. The green ring is a projection of the spherical gating shell with radii r_{sg} and r_{eg} onto the ground. (b) Side view of geometry during measurement of reference standards. Green ring depicts cross section of spherical gating shell with width w_g. According to ? the antenna's far field distances R_{ff} () are linked to the antenna's largest aperture dimension D () and wavelength λ via~~

$$R_{ff} \geq \begin{cases} 5D & : \frac{1}{3} \leq \frac{D}{\lambda} \leq \frac{5}{2} \\ \frac{2D^2}{\lambda} & : \frac{5}{2} < \frac{D}{\lambda} \end{cases}$$

The antenna aperture is rectangular with dimension $D = 0.2$, which leads to $R_{ff} \geq 1$ for 1 - 3.5 are separated from each other horizontally by $W_{ant} = 0.4$ m. The connection scheme of the VNA and the two antennas is described in Appendix B1. In Appendix B2 further details on the setup geometries can be found. During all experiments, VNA measurements were performed with a stepped $0.75 - 10.25$ GHz and $R_{ff} \geq 2.7$ frequency sweep at 3 MHz resolution (3201 points). The dwell time

230 per measured frequency was 1 μs, equivalent to a two-way travelling distance for the microwave signal of 150 m for 3.5 - 10 . Given that with all measurements the distance to the ground surface is larger than 2.7 the radiation patterns as measured by the manufacturer apply, (?). The intermediate-frequency (IF) bandwidth was minimized to 1 KHz to increase the signal-to-noise ratio.

235 The radar return from the rectangular metal plate reference target was used to calibrate the scatterometer for the co-polarization channels, as illustrated in Fig. B2(b). Radar returns from both . The two metal dihedral reflectors were measured as well. First, to enable calibration for cross polarization in the future, and second, to validate the co-polarization calibration by retrieving the dihedral reflector's radar cross sections (RCS) σ_{pp}. We worked with two dihedral reflectors, installed used as depolarizing reference targets (?) to calibrate the cross-polarization channels. We used two dihedrals, measured at different

240 distances R_c to satisfy additional requirements . Refer to Appendix ?? R_0, in order to meet requirements concerning target size, target distance (plane wave criteria), and ground-to-target interference removal. Readers are referred to Appendix B3 for the measurement details and validation-exercise results.

Time-domain filtering, or gating, was used as part of post processing to remove the antenna-to-antenna coupling and

245 undesired scattering contributions from the radar return signal for both the reference target- as the ground return and the ground-return measurements. The ring on the ground surface in Fig. B2 is the intersection of a spherical shell with radii r_{sg} and r_{eg} centred at the antennas and the ground surface. It represents the selected ground surface area for the gating algorithm: roughly put, scattering returns from features within the spherical shell remain in the radar return signal while those outside the shell are removed. The application of gating with VNA-based scatterometers is described in more detail in for example (?) or

250 (?)? or ?. Details on our gating process and related peculiarities regarding our scatterometer can be found in Appendix ??.

3.1 Experiments

During all experiments, VNA measurements were performed with a stepped $0.75 - 10.25$ frequency sweep at 3 resolution (3201 points). The dwell time per measured frequency was 1 , equivalent to a two-way travelling distance for the microwave signal of 150 . The intermediate-frequency (IF) bandwidth was minimized to 1 to increase the signal-to-noise ratio. B1.

255

In this paper, we describe the following experiments: a measurement of the In this paper, we focus on the time-series measurements of σ^0 for asphalt at various α_0 angles , measurements over a one-year period, during which measurements were taken either once or twice per hour. With this experiment, the antennas were fixed on a tower rod, such that the angle between the antenna boresight line and the ground-surface normal α_0 was 55° an the azimuth angle ϕ was fixed at 0° as shown in

Fig. 2. Although varying the antennae orientations (using automatic motorized rotational stages) to measure backscatter under various incidence- and azimuth angles would be preferable from an experimental perspective, this approach was abandoned because it would make the setup extra vulnerable to system failures. Measurements of σ^0 for different α_0- and ϕ angles at the Maqu site ~~, and finally the measurement of~~ were, however, performed during three separate days. These measurements are discussed in Section 6.3. Before installing the scatterometer at the Maqu site exploratory experiments were performed in which σ^0 over ~~a one-year period.~~ α_0 was measured for asphalt and subsequently compared to results in other studies (Sec. 6.1). Table 1 summarizes ~~the~~ all experiment geometries and dates of execution. ~~With~~ For the angular-variation experiments the scatterometer antennas were mounted on a motorized rotational stage. Depending on the angle α_0, H_{ant} would vary according to $H_{ant} = H_0 - 0.5\cos(\alpha_0)$, with $H_0 = 2.95$ or 5.2 m for the asphalt- or Maqu experiments respectively. ~~With the time-series experiment the antennas were fixed on a tower rod, such that α_0 was 55 °.~~ All angular-variation experiments were conducted within one afternoon. ~~With the time-series experiment the radar return was measured either once or twice per hour continuously.~~

Table 1. Overview of performed scatterometer experiments and their respective α_0- and ϕ ranges. Antennae aperture height H_{ant} depends on α_0.

	Date:	ϕ (°):	α_0 (°):	H_{ant} (m):
Angular variation σ_0 asphalt	4 May 2017	00	35 40 .. 75	2.55 2.55 .. 2.80
Angular variation σ_0 Maqu	25 August 2017	-20 -15 -10 -05 00 +10 +15 +20	35 40 .. 70	4.80 4.80 .. 5.05
Angular variation σ_0 Maqu	29 June 2018	-30 -20 -15 -10 -05 00 +05 +10 +20 +25 +30	35 40 .. 70	4.80 4.80 .. 5.05
Angular variation σ_0 Maqu	19 August 2018	-30 -20 -10 00 +10 +20 +30	35, 55, 70	4.80 4.90 5.05
Time series σ_0 Maqu	26 August 2017 – 26 August 2018	00	55	4.70
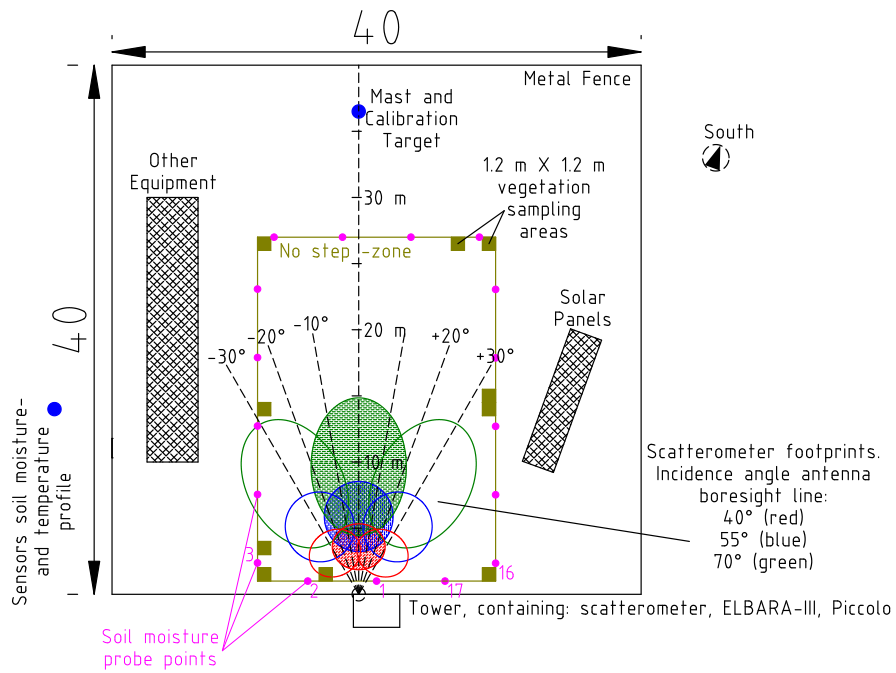
Figure 2. Map of the Maqu site. Scatterometer footprints for C-band with vv polarization are shown for different α_0- (40, 55, 70°) and ϕ (-30, -20, .., 30°) angles. For time-series measurements antennas were fixed at $\alpha^0 = 55°$ and $\phi = 0°$

4 ~~Derivation of the backscattering coefficient~~

3.1 ~~Effects of wide radiation patterns~~

3.0.1 σ^0 retrieval procedure

275 The power received by a monostatic radar- or scatterometer system from a distributed target with backscattering coefficient $\sigma_{pq}^0(\theta)$ $(\mathrm{m^2\,m^{-2}})$ is given by the radar equation (?)

$$P_{\underline{qp}}{}^{RX} = \frac{\lambda^2}{64\pi^3} P_{\underline{pq}}{}^{TX} G_0^2 \int \frac{G^2}{R^4} \sigma_{pq}^0(\theta).dA \tag{1}$$

where it is assumed that the same antenna is used for both transmitting (~~TX~~Tx) and receiving (~~RX). P_p^{TX}~~ Rx). P_q^{Tx} is the transmitted-, and ~~P_q^{RX}~~ $P_{\underline{p}}^{Rx}$ the received power respectively (W). The subscripts of the powers refers to the linear polarization

280 directions: horizontal h, or vertical v. With σ_{pq}^0 the first subscript refers to the polarization direction of the ~~incident~~ scattered- and the second to that of the ~~scattered~~ incident wave. $G\,(-)$ denotes the normalized angular gain pattern of the antenna with peak value $G_0\,(-)$. Equation 1 represents an ideal lossless system, in practice any scatterometer has frequency dependent losses or other signal distortions. These frequency dependent phase- and amplitude modulations can be accounted for by measuring the radar return of a reference target ~~P_q^c~~ $P_{\underline{p}}^c$ with known radar cross section (RCS) σ_{pq} $(\mathrm{m^2})$ (~~see Appendix. ??) and~~

285 ~~subsequently using this~~ Eq. B2) to calibrate the system. This procedure~~is~~, often referred to as external calibration. ~~Substitution of terms associated with the reference measurement into Eq. 1 leads to~~, is mathematically represented by

$$P_{\underline{qp}}{}^{RX} = P_{\underline{qp}}{}^{c} \frac{(R_c)^4}{\sigma_{pq}} \frac{(R_0)^4}{\sigma_{pq}} \int \frac{G^2}{R^4} \sigma_{pq}^0(\theta).dA \tag{2}$$

where ~~R_c~~ R_0 (m) is the distance at which the reference target was measured. In the case of a scatterometer with narrow beamwidth antenna, all integrand terms of Eq. 2 can be approximated as being constants, the so-called 'narrow-beam approxi-

290 mation' (?), so that we obtain

$$P_{\underline{qp}}{}^{RX} = P_{\underline{qp}}{}^{c} \frac{(R_c)^4}{\sigma_{pq}} \frac{(R_0)^4}{\sigma_{pq}} \frac{1}{(R_{fp})^4} \sigma_{pq}^0(\theta) A_{fp} \tag{3}$$

where A_{fp} is the scatterometers 'footprint', notably the area $(\mathrm{m^2})$ for which the surface projected antenna beam intensity is equal to or larger than half its maximum value. R_{fp} (m) refers to the distance between the antenna and footprint centre.
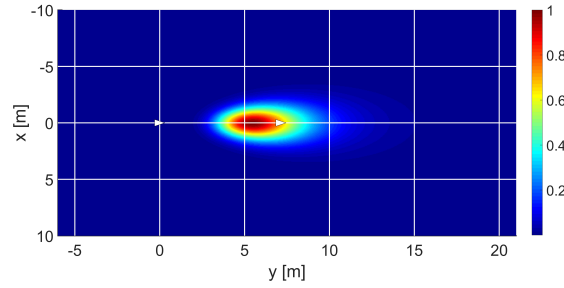
Figure 3. Example of $G^2/R^4(x,y)$ with Gaussian antenna radiation patterns. Plot normalized to its peak value. x and y are ground surface coordinates. White triangle at coordinate (0,0) represents the tower location and other white triangle indicates intersection point of the antenna boresight line and the ground surface. $\alpha_0 = 55°$, $f = 5$ GHz and polarization is vv.

For this dataset $\sigma^0_{pp}(\theta)$ $\sigma^0_{pq}(\theta)$ is estimated by employing Eq. 3 in combination with a mapping of the term $G^2/R^4(x,y)$ from Eq. 2 over the ground surface. Due to the wide antenna radiation patterns, especially with low frequencies, the area that is to be associated with the measured scatterometer signal, i.e. the footprint is typically not located where the antenna boresight line intersects the ground surface. Instead the footprint appears closer to the tower base. Figure 3 demonstrates this effect for the case of 5 GHz at $\alpha_0 = 55$ °. ~~Shown is the mapping~~, by showing the mapping of G^2/R^4 over the ground surface ~~of the G^2/R^4 term from Eq. 2.~~ This footprint-shift effect is strongest with the widest antenna radiation patterns (thus with low frequencies) and for large α_0 angles. ~~Example of $G^2/R^4(x,y)$ with Gaussian antenna radiation patterns. Plot normalized to its peak value. x and y are ground surface coordinates. White triangle at coordinate (0,0) represents the tower location and other white triangle indicates intersection point of the antenna boresight line and the ground surface. $\alpha_0 = 55°$, $f = 5$ and polarization is vv.~~ The footprint position and dimensions were found using the mapping $G^2/R^4(x,y)$ over the ground surface. The applied criterion was that the footprint contains 50% of the total projected intensity onto the ground surface. After the footprint edges were defined the incidence angle ranges were derived from them using ~~straightforward~~ trigonometry.

Because of the low ~~angular resolution~~ directivity (gain) of the antennas and ~~the~~ unknown nature of σ^0_{pq} over θ, there is an ~~uncertainty in the absolute level of~~ inherent uncertainty in our retrieved σ^0_{pq} values (for a certain θ range). ~~Quantifying this uncertainty is outside the scope of this paper. In Sec. ?? we do however provide an estimate of what this uncertainty could be.~~ ~~Despite this flaw we show that nevertheless the temporal dynamics of σ^0_{pq}, for various wavelengths, can be measured with our system.~~

3.1 ~~Implementation of the radar equation~~

~~We rewrite Eq. 3 so that the backscattering coefficient of the surface σ^0 () is related to the average received backscattered intensity $\bar{I}$ () as (?)~~

$$\sigma^0 = K^{-1}\bar{I}$$

where for brevity the polarization subscripts are omitted. The factor K () is a constant for the bandwidth considered given by

$$K = \frac{\lambda^2}{4\pi^3} I^t \frac{G^2}{R_{fp}^4} A_{fp}$$

where I^t () is the transmitted intensity by the scatterometer. For all terms in K the centre frequency is used . Similar as with Eq. 2, we can substitute I^t in Eq. C2 by the relevant radar parameters when a reference target is measured, yielding

$$K = c\epsilon_0 (E_c^{gc} - E_{bc}^{gc})^2 \frac{G(\alpha,\beta)^2}{G(\alpha_0,\beta_0)^2} \left(\frac{R_c}{R_{fp}}\right)^4 \frac{A_{fp}}{\sigma} = c\epsilon_0 (E_c^{gc} - E_{bc}^{gc})^2 \left(\frac{R_c}{R_{fp}}\right)^4 \frac{A_{fp}}{\sigma}$$

E_c^{gc} () is the measured backscattered field from the reference target (subscript c for 'calibration') and E_{bc}^{gc} () is the measured background level during calibration, i.e. the measured backscattered electric field when the calibration standard was removed from the mast while the pyramid absorbers remained in place. With both terms the superscript gc (for 'gate' during 'calibration') indicates that an identical gate was used. The prefactors light speed c () and the permittivity of vacuum ϵ_0 () convert the electric field strengths into time-average intensity. In the middle part of Eq. C3 the antenna gain functions are written explicitly. $G(\alpha,\beta)$ represents the antenna gain functions when measuring the ground return, while $G(\alpha_0,\beta_0)$ represents the situation when the radar return of the reference targets is measured. When using the narrow beam approximation (Eq. 3) and when the reference target is aligned to the antenna boresight direction the fraction becomes unity and the right part of Eq. C3 follows. The middle part is used in Appendix. ?? when alignment uncertainty of the reference targets is discussed. This matter is discussed further in Sec. 6.2.

~~In the context of Rayleigh fading statistics with square-law detection (?), the average received intensity $\bar{I}$ ()is linked to I_N (), which is the measured intensity averaged over N independent samples (N footprints or N frequencies), according to~~

335 $\bar{I} = \dfrac{I_N}{1 \pm 1/\sqrt{N}}$

~~Note that $\bar{I}$, like σ^0 is an implied ground surface property. The quantity that is actually measured, I_N, is an estimator for $\bar{I}$. Equation C4 holds for $N \geq 10$, since then the probability density function of I_N approaches a Gaussian distribution (?) according to the central limit theorem. The denominator in Eq. C4 represents a 68% confidence interval (± 1 standard deviation) for $\bar{I}$. More details on fading are described in Section C2.~~

~~I_N is calculated from the measured~~ In Figure 4 the procedure for deriving the backscattering coefficient is depicted. The
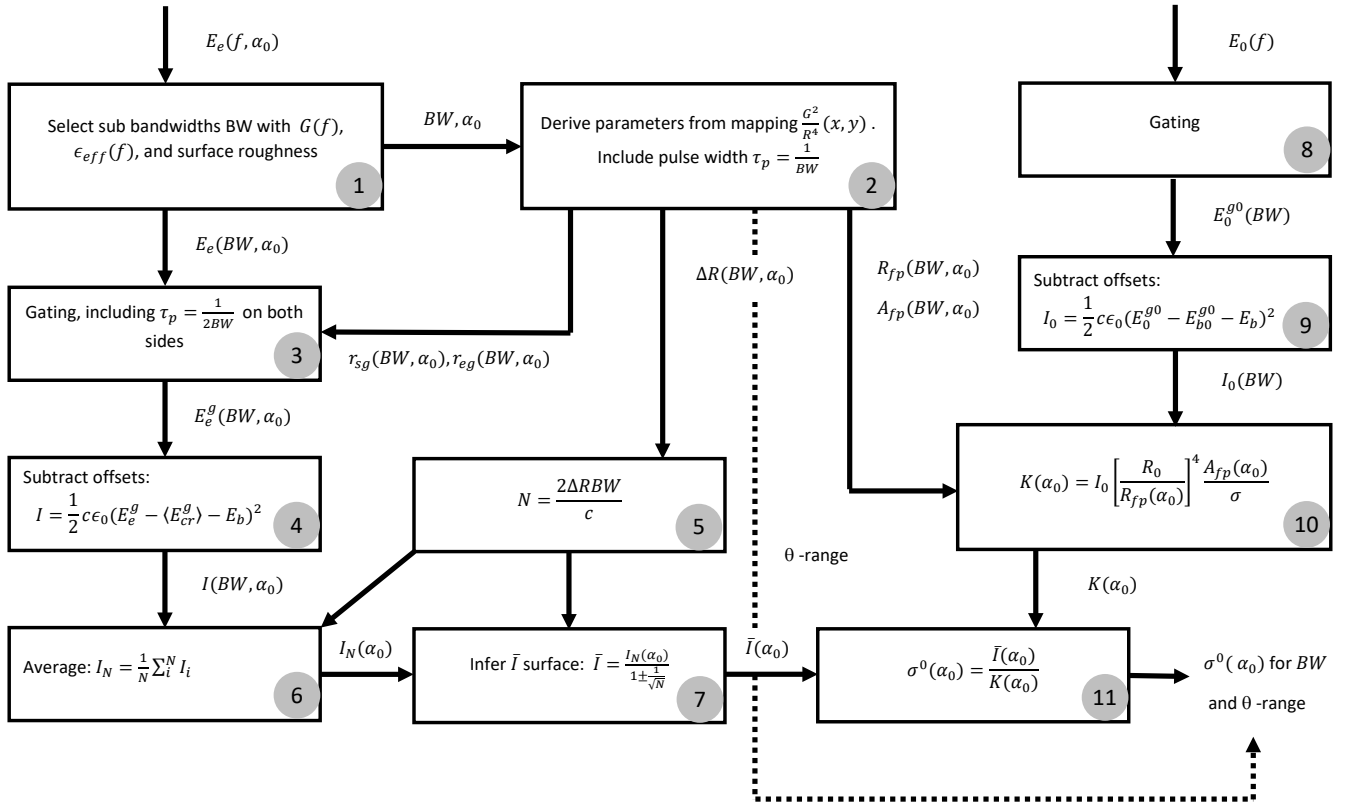
Figure 4. Flowchart of σ^0 derivation process. Inputs are the measured backscattered electric fields of the surface target $E_e(f, \alpha_0)$ and the calibration standard $E_0(f)$. The process follows from 1 to 11 in sequence.

340

equations used therein are derived from Eq. 3. Refer to Appendix C1 for more information. The different steps indicated in the figure are explained here:

1. We start with E_e (V m^{-1}), the measured backscattered electric field from the ground target incident on the receiving antenna E_e^g () by

$$I_N = c\epsilon_0 \frac{1}{N} \sum_{i=1}^{N} (E_e^g(f_i) - E_n^g(f_i))^2$$

. The subscript e denotes 'envelope' magnitude of the complex signal, as in (?)[1] and the superscript g indicates that the signal is gated. E_n^g () is the measured electric field with the antennas pointing skywards and thus represents the scatterometer's 'noise' level. Note that the exact gate is applied as with E_e^g.

3.1 Fading and bandwidth selection

Fading is the phenomena that radar return of a distributed target with uniform electromagnetic properties has varying magnitudes and phases when different locations or slightly different frequencies are measured (?), (?). To remove this varying nature from a surface-classifying quantity like σ_{pq}^0 averaging must be performed. By definition σ_{pq}^0 is the average radar cross section of a certain type of distributed target, e.g. forest, asphalt, wheat field, normalized by the illuminated physical surface area. σ^0 is proportional to the average measured received power P^{RX} (Eq. 3) or intensity $\bar{I}$. Therefore, determining $\bar{I}$ and σ^0 requires N statistically independent samples so that the sample average I_N approaches the actual average $\bar{I}$ proportionally to $1/\sqrt{N}$ in accordance with the central limit theorem.

Practically, this can be done either by measuring I at N different locations over the surface, called spatial averaging, or with the frequency averaging -technique (see for example (?)). With the latter, physical properties governing the scattering, permittivity and surface roughness are considered frequency invariant over a certain bandwidth. Subsequently, N different frequencies should be selected according to some criteria that accounting for fading. Both averaging techniques can be used simultaneously as done by ? to increase the total number of independent samples. We solely applied the frequency-averaging technique because during the time-series measurements our antennas were in a fixed position and orientation. We assumed the single footprint area to be representative for the whole surface of the Maqu site. In Sec. 6.3 we show this assumption is justified. The used method for finding the number N of statistically independent samples within a bandwidth is described in ?:

$$N = \frac{2BW\Delta R}{c}$$

where $\Delta R = r_{sg} - r_{eg}$. Subsequently, with $N-1$ intervals of Δf (), N frequencies are selected from within BW.

As indicated above, with the application of the frequency averaging technique it is assumed that the backscatter behaviour across the selected BW is uniform. To assess the validity of this assumption for bare surface, the improved integral equation method (I^{2}EM) surface scattering model (?) is applied using the roughness parametrization reported in ? and a (frequency-dependent) effective dielectric constant $\epsilon_{soil}(f)$ according to the dielectric mixing model by ?.

---

[1]In reality the measured fields or signals remain complex until after the gating process. We however stick to this terminology for clarity.

~~Over a BW the mean value $\langle\sigma^0(BW)\rangle$ is calculated, followed by the ratios $\sigma^0(BW_{lo})/\langle\sigma^0(BW)\rangle$ and $\sigma^0(BW_{hi})/\langle\sigma^0(BW)\rangle$ to quantify the change of σ^0 over the BW. In general the I²EM model predicts that the change is largest for long- and smallest for short wavelengths and that it is largest for hh polarization and smallest for vv polarization. Furthermore, the RMS surface height is the most sensitive target parameter. Variation of σ^0_{hh} per BW calculated with combined I²EM (?) and Dobson (?) model. Horizontal axis shows centre frequency of bandwidth $BW = 0.5$. Curves indicate the values (in) to be added to $\langle\sigma^0_{hh}(BW)\rangle$ at edges of BW for different θ angles. Shown calculation uses: $s = 1$, $\ell = 10$, $m_v = 0.25$, and $T_{soil} = 15$. As an example, figure C1 shows the calculation result for hh polarization with a BW of 0.5. From the graph we can read that for a centre frequency of 2.75 that the retrieved σ^0_{hh} for that BW can be expected to vary $+1.0$ to -1.2 for $\theta = 50°$.~~

~~Based on the above calculations we chose $BW = 0.5$ for S-, and C-band and $BW = 1.0$ for X-band. These bandwidths will lead to N-values around 15 which is sufficient to let the probability density function of I_N approach a Gaussian distribution. as explained in Sec. ??. Further increment of BW was considered not to outweigh the loss of frequency resolution, especially at S-band.~~

3.1 ~~Procedure~~

~~In Figure 4 the procedure for deriving the backscattering coefficient is depicted. The different steps indicated in the figure are explained here: Flowchart of σ^0 derivation process. Inputs are the measured backscattered electric fields of the surface target $E_e(f, \alpha_0)$ and the calibration standard $E_c(f)$. The process follows from 1 to 11 in sequence.~~

2. ~~We start with E_e measured over the~~ This quantity is measured over the full $0.75 - 10.25$ GHz band at angle α_0: $E_e(f, \alpha_0)$. Bandwidths BW are selected based on the change of $G(\alpha, \beta)$ over frequency (Appendix ~~??~~B1), the number of independent frequency samples N that may be retrieved from BW, and the estimated change of backscattering properties over frequency of the ground surface as is discussed in ~~Sec.~~ Appendix C2. Result is the bandwidth selection $E_e(BW, \alpha_0)$.

3. With BW and α_0 as input, $G^2/R^4(x, y)$ is mapped for all frequencies within BW using the antenna radiation patterns measured by the manufacturer. The region associated with 50 % of the total projected intensity onto the ground is determined to set appropriate gating times, or distances ~~r_{gs}, r_{ge}~~ r_{sg}, r_{eg}, and for calculating the A_{fp}, R_{fp}, and the θ range. Half the pulse width $c/(2BW)$ is subtracted from ~~r_{gs}~~ r_{sg} and added to ~~r_{es}~~ r_{eg}, quantities A_{fp}, R_{fp}, and the θ range are changed accordingly.

4. The gate is applied to $E_e(BW, \alpha_0)$, resulting in the gated backscattered field $E_e^g(BW, \alpha_0)$, where the superscript g indicates that the signal is gated.

5. The ~~noise level signal $E_n^g(BW)$ is~~ bandwidth-average coupling remnant $\langle E_{cr}^g \rangle$ and minimal detectable signal E_b are subtracted from $E_e^g(BW, \alpha_0)$ for each measured frequency. ~~The~~ E_{cr}^g (V m^{-1}) is an offset formed by part of the signal transmitted from the transmit antenna coupling directly into the receive antenna (antenna cross coupling). Although

the majority of this coupling can be filtered out by using time-domain gate filtering, a remnant is still present (hence 'coupling remnant' in the subscript) and must be accounted for (Appendix E4). Note that the same gate as with E_c^g is

405   applied. A similar form of offset subtraction from E_c^g was done in for example ?. Next, result is squared and converted into intensity $I(BW, \alpha_0)$.

6. To reduce the radiometric uncertainty due to fading we perform frequency averaging. The number of statistically independent frequency samples N within BW is calculated with $\Delta R = r_{ge} - r_{gs}$ (Sec. C2) $\Delta R = r_{cg} - r_{sg}$. Please refer to Appendix C2 for more information.

410 7. From the $I(BW, \alpha_0)$ spectrum N intensities are selected at equidistant intervals of $\Delta f = BW/N - 1$ and averaged to $I_N(\alpha_0)$.

8. With $I_N(\alpha_0)$ and N, the average received intensity $\bar{I}(\alpha_0)$ (W m^{-2}) is calculated using Eq. C4. The denominator $1 \pm 1/\sqrt{N}$ implies that $\bar{I}$ is estimated with a 68 % confidence interval.

9. The gated backscattered signal from the reference target $E_c^{gc}(BW)$ $E_0^{g0}(BW)$ (V m^{-1}) (subscript 0 represents 'reference',

415   superscript $g0$ stands for 'gate' during reference measurements) is determined for the full 0.75 – 10.25 GHz band under the assumption that $G \approx 1$ for all frequencies (see Appendix ??B1). After gating the relevant BW of E_c^{gc} E_0^{g0} is selected.

10. The measured response from the mast without reference target $E_{bc}^{gc}(BW)$ $E_{b0}^{g0}(BW)$ is subtracted from the reference target response. Subscript bc $b0$ denotes background calibration, the superscript gc $g0$ indicates that the same gate was

420   used as with the reference target response. Also E_b is subtracted here. The result is squared and converted into intensity $I_c(BW)$ $I_0(BW)$ (W m^{-2}).

11. The $I_c(BW)$ $I_0(BW)$ is used to calculate the factor K (W m^{-2}), given the footprint area A_{fp} and centre distance R_{fp} (Eq. C2).

12. The final step is the application of Eq. C1 with $\bar{I}(\alpha_0)$ and $K(\alpha_0)$ as inputs to obtain σ^0. By steps 2 and 6 the derived σ^0

425   is to be associated with the chosen BW and calculated θ -range. By step 7 a 68 % confidence interval applies to σ^0.

4   Measurement results

4.1   ~~Measurement uncertainty~~

For the analyses in this paper we discuss results of four bandwidths BW, picked amidst frequency ranges typically used in microwave remote sensing: 9 – 10 GHz (X-band), 4.5 – 5 GHz (C-band), 2.5 – 3 GHz (S-band), and 1.5 – 1.75 GHz (L-band).

430 The widths decrease with wavelength due to the expected frequency resolution of the target's scattering response (Appendix C2) and the antenna-radiation-pattern change over frequency (Appendix B1). Presented in this section is first, a global overview

of the retrieved σ_{pq}^0 over the period 26 August 2017 – 26 August 2018, followed by a 13-day time-series of σ_{pq}^0 at the highest temporal resolution during the thawing-period in April 2018.

4.0.1 ~~Fading- and systematic measurement uncertainty~~

~~Besides uncertainty due to fading, systematic measurement uncertainty was also considered in the retrieval~~ Figure 5 presents an overview of the time-series data of σ_{pq}^0 over the whole August 2017 – 2018 period for all considered bandwidths in L-, S-, C-, and X-band, along with M_v, T_{soil} at four depths ranging from 2.5 to 20 cm and precipitation. Based on observed albedo values, days at which a layer of snow was present are indicated. For visibility reasons the graphs only display measurements taken at 18:10 with 2 day intervals and one cross-polarization channel (σ_{vh}^0 and σ_{hv}^0 are within each others confidence intervals.) Data of the radar return and σ_{pq}^0 for November 2017 is not available, while that of late June – Early July 2018 will become available at a later stage.

We observe for all bands and polarizations that σ^0 is highest in summer and autumn while it is lowest during winter. The same observations were made with satellites over the Maqu area for L-band (?) and C-band (?). This behaviour can be explained by the fact that in summer and autumn M_v, and the amount of fresh biomass is highest. As a result, the high dielectric constant of moist soil, in combination with the rough surface and presence of water in the vegetation results in strong backscattering. During winter, however, there is little liquid water, i.e. M_v, present in the soil and no fresh biomass (dry biomass however remains present, see Fig. A1). Black arrows indicate frozen- and thawed soil at 25 cm depth (Appendix A2). The dielectric constant of the soil therefore is lower compared to that of moist soil and there is little to no scattering from the dried out vegetation, resulting in a lower σ_{pq}^0. All aforementioned effects are described in, for example, (?). There were, however, also peaks of σ_{pq}^0 during winter, for example on 26 January, which coincided with snowfall. In (?) strong backscatter increments due to fresh snowfall was also observed for X-band. Apparently, this behaviour is similar with the longer wavelengths as the graphs show.

When comparing the four bands we observe that, in general, the backscattering is highest for X-band and lowest for L-band or S-band. This difference is mainly driven by the wavelength-dependent response to the surface roughness of the soil and vegetation during the summer and autumn period. For longer wavelengths the soil surface roughness appears smoother than for the shorter wavelengths, resulting in stronger specular reflection, thus lower backscatter. A similar argument holds for the vegetation: its constituents are small compared to the longer wavelengths, thus little volume scattering occurs. Except for during the summer, backscatter for vv polarization was equal to, or higher than that for hh polarization. This behaviour was also observed by ?, albeit for bare soil. We however may compare our situation to that of bare soil during winter, when there is no fresh biomass. When vegetation was present, σ_{hh}^0 was stronger for all bands, as is visible during June - August 2018. This was however not the case during August - September 2017, when the vegetation probably still contained water. Somewhat stronger backscatter, $0.5 - 1$ dB, for hh- than for vv polarization was also reported for grassland in ? with $40 \le \theta \le 60°$ for S- and X-band. For C-band they reported no clear difference. Yet another study, (?), measured 3-4 dB higher backscatter for hh- than for vv polarization when measuring wheat at L-band ($\theta = 40°$). Our results for L-band were similar. Cross polarization

σ^0 levels were, as expected, lower than those of co polarization. During winter period this difference was largest, especially with C-band. For L-band, on the other hand, this difference in σ^0 levels between co- and cross polarization was quite small.
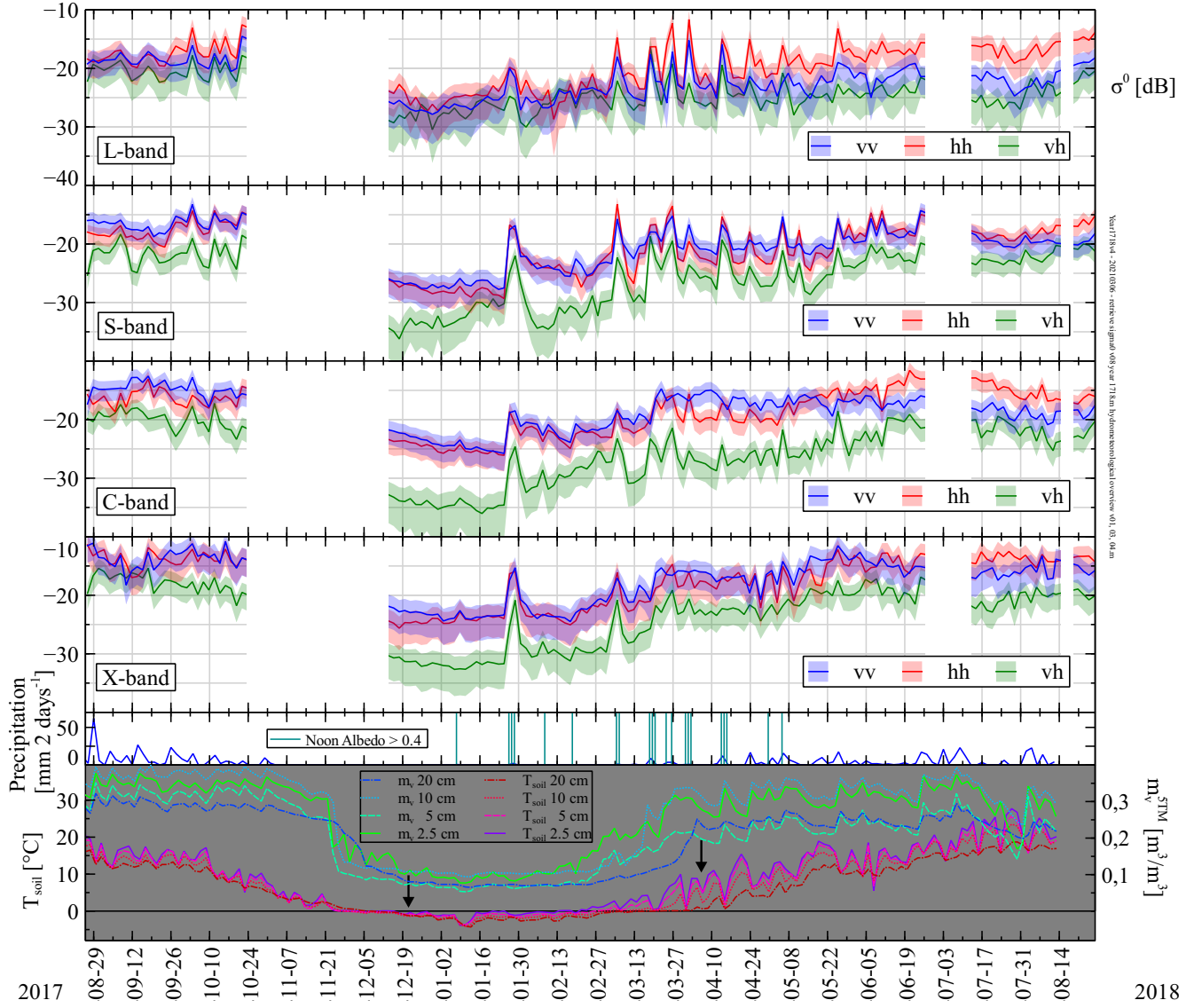
Figure 5. Time-series measurements of σ_{pq}^0 ($m^2 m^{-2}$) for L-, S-, C- and X-band, M_v and T_{soil} from August 2017 to 2018. Shown are measurements taken at 18:10 with 2 day intervals. Shaded regions indicate 66% confidence intervals for σ_{pq}^0. Antenna boresight angle fixed at $\alpha_0 = 55°$. The incidence angle ranges are band- and polarization dependent. Widest ranges are: L-band: $0° \le \theta \le 60°$, S-band: $20° \le \theta \le 60°$, C-band: $36° \le \theta \le 60°$, and X-band: $47° \le \theta \le 59°$. Bottom graphs show measured precipitation per 2 days (snowfall identified by noon albedo), volumetric soil moisture m_v^{5TM} ($m^3 m^{-3}$) and soil temperature T_{soil} at indicated depths. Arrows indicate frozen/thawed soil at 25 cm. Spatial average volumetric soil moisture M_v is estimated as $M_v = m_v^{5TM} \pm 0.04$ $m^3 m^{-3}$.

Next, four 13-day time-series of σ^0 ~~. The radar returns and subsequent~~ at 30-minute intervals are presented. When selecting these periods we tried avoiding strong precipitation events as much as possible, since these complicate the interpretation. In Appendix D time-series during October 2017 (Fig. D1), December 2017 (Fig. D2) and July 2018 (Fig. D3) can be found. Here we shall describe the retrieved σ^0_{pq} during 13-day period in April 2018 (Fig. 6) when the thawing process was ongoing.

The most prominent features in Fig. 6 are the diurnal variations of σ^0_{pq} that are clearly caused by changes of M^v. For S-, C-, and X- bands we observe that σ^0 ~~values derived from it have a systematic measurement uncertaintywhose main contributors are~~ increases during daytime due to the increase of liquid water in the top soil due to thawing and at night σ^0 drops as most of the water freezes again. For L-band this behaviour is also visible, though not as pronounced. The M_v changes at different depths are consistent with this difference: the strongest diurnal variation in liquid water was measured by the probes at 2.5 and 5 cm depth while those at 10 and 20 cm do not change as much. On some days, for example 4 and 5, or on 10 April, we observe diurnal changes in σ^0 (most pronounced for X-band) while the M_v measured by the 5TM sensors at 2.5 and 5 cm depth showed little variations. This may suggest that the freezing and thawing during those days occurred only in the very top-soil layer, just below the air-soil interface where it was outside the influence zone of the 5TM sensors. The time lag between the drop of σ^0 (first) and the drop of 5TM M_v (second), is caused by the same phenomena as the freezing starts at the top soil layer and progresses downward. The time lag during thawing was smaller. In general the magnitude of the σ^0 -change was largest for X-band and smallest for L-band, though exceptions exist. See for example 3 April, where for L-band σ^0_{hh} drops almost 10 dB, which is more than for other bands. At the same time M_v at 20 cm depth also shows strong variation, while M_v at 10 cm changes less.
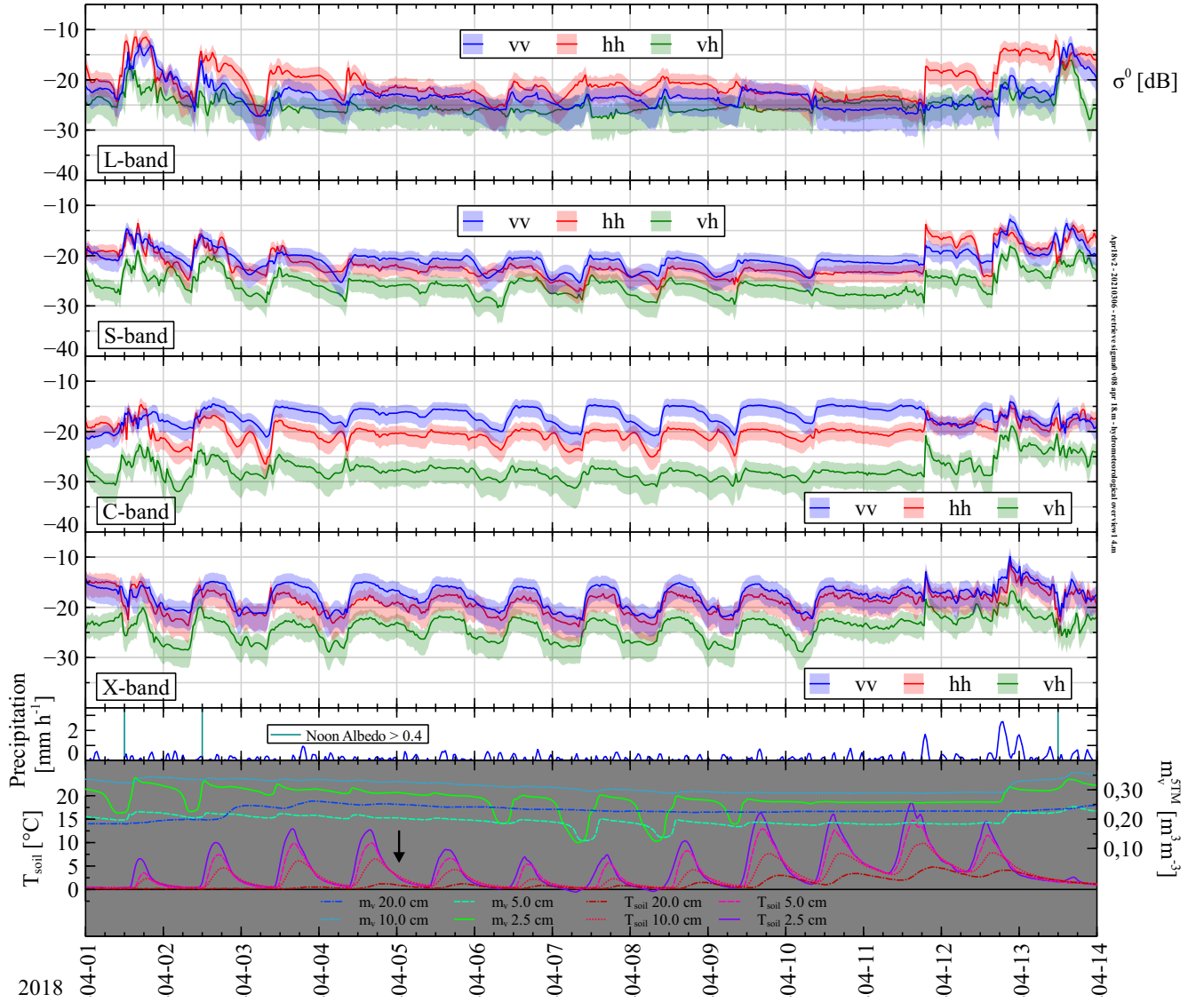
Figure 6. Time-series measurements of σ_{pq}^0 (m^2 m^{-2}) for L-, S-, C- and X-band, precipitation, M_v and T_{soil} during 13 days in April 2018. Shaded regions indicate 66% confidence intervals for σ_{pq}^0. Antenna boresight angle fixed at $\alpha_0 = 55°$. The incidence angle ranges are band- and polarization dependent. Widest ranges are: L-band: $0° \leqslant \theta \leqslant 60°$, S-band: $20° \leqslant \theta \leqslant 60°$, C-band: $36° \leqslant \theta \leqslant 60°$, and X-band: $47° \leqslant \theta \leqslant 59°$. Bottom graphs show measured precipitation (mm hr^{-1}) (snowfall identified by noon albedo), volumetric soil moisture m_v^{5TM} (m^3 m^{-3}), and soil temperature T_{soil} at indicated depths. Arrow indicates thawing of soil at 25 cm. Spatial average volumetric soil moisture content M_v is estimated as $M_v = m_v^{5TM} \pm 0.04$ m^3 m^{-3}.

5 Code and data availability

In the DANS repository, under the link https://doi-org.ezproxy2.utwente.nl/10.17026/dans-zfb-qegy the collected scatterometer data is publicly available (**?**). Stored are both the radar-return amplitude and phase for all four linear polarization combinations and processed σ^0_{pq} for the L-, S-, C-, and X-band bandwidths discussed in this paper. The dataset includes time-series measurements from 26 August 2017 – 26 August 2018, data of angular variation experiments, and radar returns of the reference targets. Accompanying data includes time-series measurements of soil moisture and -temperature profile at depths of [2.5, 5.0, 7.5, 10, ...90, 100 cm], as well as time-series measurements of air temperature, precipitation and up- downward short- and long wave irradiation. Also, in the DANS repository under https://doi-org.ezproxy2.utwente.nl/10.17026/dans-xyf-fmkk (**?**) Matlab scripts are available for processing measured radar return data and for retrieving σ^0_{pq} for other bands within the measured 1 – 10 GHz frequency range.

6 Discussion

6.1 Reference measurements for asphalt

In order to check our scatterometer setup- and σ^0-retrieval procedure an experiment was performed in which the backscatter of asphalt was measured and subsequently compared to results found in other studies. This exercise is described in Appendix F. We found our results for X-band with co-polarization and S-band for vv- and vh polarization to match with those reported in **?** and **?** respectively. For L-band a proper comparison was not possible due to the width of our antenna patterns. We could not find other studies reporting backscatter for C-band to compare our results to.

6.2 Measurement uncertainty

In the derivation of σ^0 we distinguish four sources of uncertainty: *(i)* Fading (Sect. 3.0.1), *(ii)* the temperature-induced radar return uncertainty ΔE^g_T ()and ΔE_T (V m^{-1}), *(iii)* reference target measurement uncertainty ΔK ()in dB, as it is relative value) and *(iv)* the low-directivity-induced uncertainty.
First we describe *(ii)* and *(iii)*, which are systematic sources of uncertainty. For both factors we estimate their respective uncertainty levels (see Appendix **??** and Appendix **??** respectively) and how these propagate into an overall σ^0 measurement uncertaintytogether with the fading uncertainty. In this context we also consider here the system's noise floor E^g_n and the Noise Equivalent σ^0 (NES)derived from it, (see Appendix **??**) offsets levels formed by the antenna-to-antenna coupling remnant E^g_{cr} (V m^{-1}) and the minimum signal strength measurable by the VNA, or background E_b (V m^{-1}). The former is derived from measurements with the antennas aimed skywards. From E_b the minimum measurable RCS (given a certain distance R to target) σ_{min} can be calculated via Eq. 3, where instead of the product $\sigma^0 A_{tp}$ a RCS value is to be calculated using the power levels associated with E_b. Appendix E contains detailed information on all considered systematic sources of uncertainty and offsets, starting with an overview (Appendix E1), followed by sections on ΔE_T (Appendix E2), ΔK (Appendix E3), and $E^g_{cr}(f)$ (Appendix E4).Table E1 lists all estimated systematic uncertainties and noise floor levels.

This table is modified and moved to Appendix E2

Starting with Eq. C1 it can be shown (see Appendix ~~??~~E5) that the three estimated types of uncertainty, namely fading, ~~temperature-induces~~ temperature-induced radar return uncertainty (~~ΔE_T^g~~ΔE_T), and reference target measurement uncertainty (ΔK) can be combined in a model for total σ^0 uncertainty:

$$\sigma^0 = \frac{I_N \pm \Delta I_N}{(K \pm \frac{2}{3}\Delta K)(1 \pm 1/\sqrt{N})} = \frac{I_N}{K} \pm \Delta\sigma^0 \tag{4}$$

ΔI_N (W m^{-2}) is a statistical error that follows from ~~ΔE_T^g~~ΔE_T, ΔK is converted from a maximum possible error into a statistical error with a $(2/3)$ probability confidence interval and the term $1/\sqrt{N}$ represents a statistical error caused by fading. In the right term the three uncertainty contributions are merged into one statistical uncertainty $\Delta\sigma^0$ (m^2 m^{-2}), which is a 66% confidence interval for σ_0. In this paper these 66% confidence intervals are presented in all figures showing our retrieved σ^0. To give an indication of the magnitude of $\Delta\sigma^0$, ~~which are different per bandwidth, polarization , and overall σ^0-level, some extremes~~ some typical values over band, polarization and season are summarized in Table 2. ~~Shown~~ Presented values were retrieved from the calculated time-series results ~~, which are presented in Section ??.Example uncertainty values $\Delta\sigma^0$ () per bandwidth, polarization, and overall σ^0-level.~~ of Section 4.

6.2.1 ~~Uncertainty due to angular resolution antenna patterns~~

~~Measuring the dependence of σ^0 on incidence angle θ,~~ The low-directivity-induced uncertainty *(iv)* is not quantifiable in the sense that with the time-series experiments backscatter was not repeatedly measured at different α_0 angles. With such measurements, sets of $P_q^{RX}(\alpha_0)$ would be obtained that can be deconvolved into $\sigma^0(\theta)$~~, with a scatterometer whose antenna radiation patterns are $G(\alpha,\beta)$ is equivalent to the convolution of $\sigma^0(\theta)$ with $G(\alpha[\theta],\beta[\theta])$. For a narrow-beamwidth antenna $G(\alpha[\theta],\beta[\theta])$ may be approximated by a block-function whose width is the FWHM beamwidth. This is equivalent to the narrow-beam approximation mentioned in Sec. ??, the measured 'convolved' $\sigma^0(\theta)$ is similar to the 'actual' $\sigma^0(\theta)$. With antennas whose FWHM beamwidths probably exceed the rate of change of σ^0 over θ this approximation will lead to larger errors. Still, in principle it is possible to deconvolve the convoluted $\sigma^0(\theta)$ function to obtain the actual $\sigma^0(\theta)$~~, since $G(\alpha,\beta)$ is known ~~. This deconvolution is performed by?~~ (see Eq. 2). This deconvolution approach was performed by, for example, ~~but~~

Table 2. Example uncertainty values $\Delta\sigma^0$ (dB) per bandwidth, polarization, and overall σ^0-level.

	L-band	S-band	C-band	X-band
High σ^0-levels (typical in summer)				
vv	+1.6 – -2.5	+1.3 – -1.9	+1.4 – -2.1	+1.7 – -3.0
vh	+1.7 – -3.0	+1.3 – -1.9	+1.4 – -2.2	+1.6 – -2.7
hv	+1.8 – -3.2	+1.3 – -1.9	+1.4 – -2.0	+1.6 – -2.7
hh	+1.6 – -2.5	+1.2 – -1.7	+1.3 – -2.0	+1.7 – -2.9
Low σ^0-levels (typical in winter)				
vv	+2.3 – -5.2	+1.9 – -3.7	+1.7 – -2.9	+2.1 – -4.2
vh		+2.4 – -5.9	+2.6 – -8.3	+2.3 – -5.2
hv	+2.4 – -6.0	+2.5 – -6.6	+2.5 – -6.4	+2.0 – -4.9
hh	+2.3 – -5.3	+1.7 – -2.8	+1.7 – -2.7	+1.9 – -3.8

was considered to be outside the scope of this paper. Instead, the procedure as explained in Sec. ?? was followed which, consequently, does result in an unknown uncertainty in the retrieved σ^0. ? and ?. It is possible, however, to estimate this uncertainty give an estimate of the low-directivity-induced uncertainty, inherent to our σ^0 retrieval method, with a simple numerical experiment in which the scatterometer radar return is simulated (Eq. 2) using a pre-defined functional type of

Table 2. Example uncertainty values $\Delta\sigma^0$ (dB) per bandwidth, polarization, and overall σ^0-level.

	L-band	S-band	C-band	X-band
High σ^0 -levels (typical in summer)				
vv	+1.6 – -2.5	+1.3 – -1.9	+1.4 – -2.1	+1.7 – -3.0
vh	+1.7 – -3.0	+1.3 – -1.9	+1.4 – -2.2	+1.6 – -2.7
hv	+1.8 – -3.2	+1.3 – -1.9	+1.4 – -2.0	+1.6 – -2.7
hh	+1.6 – -2.5	+1.2 – -1.7	+1.3 – -2.0	+1.7 – -2.9
Low σ^0 -levels (typical in winter)				
vv	+2.3 – -5.2	+1.9 – -3.7	+1.7 – -2.9	+2.1 – -4.2
vh	+2.3 – -5.2	+2.4 – -5.9	+2.6 – -8.3	+2.3 – -5.2
hv	+2.4 – -6.0	+2.5 – -6.6	+2.5 – -6.4	+2.0 – -4.9
hh	+2.3 – -5.3	+1.7 – -2.8	+1.7 – -2.7	+1.9 – -3.8

New Table 2

555 function for $\sigma^0(\theta)$. We ~~used~~ may use for example the empirical model ~~of~~ $\sigma_{pq}^0(\theta)$ for grassland developed ~~by ?. When using our retreival method~~ in ? with measurement data from several other studies. Applying the method of Sec. 3.0.1 on the simulated ~~scatterometer~~ radar return we obtain, for 4.75 GHz ~~with~~ at vv polarization $\sigma_{vv}^0 = -14.4$ dB for $34° \leq \theta \leq 60°$, while the actual value over this interval varies from $-13.0 \leq \sigma_{vv}^0 \leq -14.9$ dB. Although this discrepancy depends on the (unknown) form of $\sigma^0(\theta)$, in general this error will be larger for low- and smaller for high frequencies because of the respective antenna

560 beamwidths ~~.~~

6.3 ~~Measured backscattering coefficients~~

~~For the remaining analysis we discuss the results for three bandwidths: 9 − 10 (X-band), 4.5 − 5.0 (C-band), and 2.5 − 3.0 (S-band). These are chosen because their respective wavelengths are doubled with respect to each other: 3.0 − 3.3 , 6.0 − 6.6 , and 10 − 12 .~~

565 **6.2.1** ~~**Angular variation σ_{pp}^0 asphalt**~~

~~We start with the asphalt experiment result, which we present here to demonstrate that our~~ and has to be kept in mind when using the ~~σ^0 retrieval method, using measurement data obtained with our scatterometer system, results in σ^0~~ -values ~~comparable to those in other studies~~ of this dataset. Despite this uncertainty, the σ^0 retrieved in this dataset nevertheless does show all relevant temporal dynamics that are furthermore wavelength- and polarization dependent.

570

~~The co-polarization backscattering coefficients over various angles α_0 are shown in Fig. ??. The results are plotted together with curves of the empirical model of $\sigma_{pq}^0(\theta)$ for asphalt described in ?. This model was developed by using measurement data of numerous previous studies on asphalt backscattering. Measurement results of $\sigma_{pp}^0(\alpha_0)$ for asphalt within 9 - 10 band vs. Ulbay's empirical model ?. Points represent measurement results for different antenna boresight angles α_0. Horizontal bars~~

575 ~~represent intervals for angle of incidence θ and vertical bars the 66% confidence interval for σ^0. Dotted lines between data points are guide to the eye. Solid and dotted curves (green and cyan) represent mean value and 90% confidence interval of empirical model respectively. For both vv- and hh polarization the measured data shows a clear overall decreasing trend of~~ Alternatively, the low-directivity-induced uncertainty can be avoided by using the radar return of the dataset P_p^{Rx} together with a microwave scattering model instead of the retrieved σ^0 ~~over θ, which is expected from a surface that is smooth compared~~

580 ~~to the wavelength. Overall, σ^0 for vv polarization is higher than for hh polarization, which is in accordance to the empirical model . Starting from the smaller angles, the consecutive measurement points remain at similar level. With hh polarization there appears to be even a local minimum at $40°$, although the measurement uncertainty is relatively large there. Given that the empirical curves show a similar trend , though not as pronounced, the slow decay of σ_{pp}^0 over θ for $25 − 55°$ can simply be a property of asphalt. Overall we find our measurements to lie within the 90 % occurrence interval of the empirical model and,~~

585 ~~therefore, conclude that our results for asphalt are similar to the experiments used by ?.~~ The angle-dependent $\sigma_{pq}^0(\theta)$ then may be obtained by the microwave scattering model and simply applied in Eq. 2 to simulate the radar return, which subsequently can be compared to the measured P_p^{Rx} values.

6.2.1 ~~Angular variation σ^0_{pp} Maqu~~

6.3 Angular variation of σ^0_{pq} in Maqu

~~With the scatterometer experiments where the radar return~~ Next, we present the measurement results and analysis of the angle-dependent backscatter of the Maqu-site surface ~~was measured at various antenna boresight- (α_0) and azimuth (ϕ) angles we intent to achieve the following~~ for two purposes. First, we present it to quantify the behaviour of σ^0 with respect to the elevation angle (θ), BW, and polarization channels for the Maqu site ground surface with a living vegetation canopy. ~~Second, to asses~~, and second, to assess the spatial homogeneity of $\sigma^0(\theta)$ over the Maqu-site surface by also measuring backscatter at different azimuth angles (ϕ). As explained in ~~Sec.~~ Appendix C2, the single footprint area for the σ^0 time-series measurements should be representative for the whole Maqu-site surface.

Due to practical limitations of possible ϕ angles and because of the wide antenna beam widths, the footprints of used α_0- and ϕ combinations in this experiment overlap partially, as is shown in Fig. 2~~)~~. However, since we employ frequency averaging to reduce the fading uncertainty for every footprint, we argue that the σ^0 -values retrieved per (overlapping) footprint may nevertheless be compared to each other for this section's analysis.

~~Figures ?? and ?? show measured backscattering coefficients for different α_0- and ϕ angles for X- and for S-band respectively. There is a clear tendency of σ_0 decreases with α_0. Deviations from this trend, for example with X-band at $\phi = 10°$, $\alpha_0 = 50°$, might point to local strong scattering, but could also simply be due to fading. Since the S-band response for the same ϕ shows a clear decreasing trend of σ_0 over α_0 it is probably the latter.~~

~~Measurement of $\sigma^0_{hh}(\alpha_0,\phi)$ for 9.0 - 9.9 sub band over Maqu site on 20170825. Main figure: For different antenna boresight azimuth angles ϕ σ^0_{hh} over boresight elevation angles α_0 is shown. The 8 vertical bars represent the 66% confidence interval for σ^0. Intervals for incidence angles θ per measurement are not shown here for clarity of figure. Inset: $\sigma^0_{hh}(\alpha_0)$ for $\phi = 0°$. Horizontal bars represent intervals of actual incidence angles θ. Measurement of $\sigma^0_{vv}(\alpha_0,\phi)$ for 2.5 - 3.0 sub band over Maqu site on 20170825.~~ As a means to quantitatively evaluate the σ^0 behaviour with respect to θ- and ϕ angle the data is grouped in sets of σ^0 over α_0 for every angle ϕ, BW, and polarization. In Appendix G, Fig. G1 examples of such sets are shown. Next, an iterative least-squares non-linear fitting algorithm is applied to fit each set to the model

$$\sigma^0 = A\cos(\theta)^B \tag{5}$$

where A is a constant $(\mathrm{m}^2\,\mathrm{m}^{-2})$ and B is either 1 for an isotropic scatterer or 2 for a surface in accordance with Lambert's law (**?**). ~~Since the retrieved~~ For each α_0 we find the coordinate for which G^2/R^4 is maximum and use that position's angle of incidence θ together with the centre σ^0 ~~values are in fact~~ value of the 66% confidence interval for σ^0, ~~we used the centre σ^0 -values for the~~ the fitting process. ~~Figure 7 shows the A coefficients found for both values of B.~~ As a next step, we reduced the number of fitting possibilities by selecting for each polarization-BW combination the most likely value for B (1 or 2). This was done by tallying over the ϕ -angles which of the two fitted curves $\sigma^0 = A\cos(\theta)^B$ passed through the confidence intervals best and had the highest coefficients of determination (R^2)~~(numbers in Fig. 7).~~. The outcome was $B = 1$ for all polarization channels of X-band ~~vv- & hh polarization~~, and $B = 2$ for all of S-, and L-band. For C-band ~~hh~~ it was harder to judge in

favour of either. We chose $B = 1$ for vh polarization and $B = 2$ for vv, hh, and hv. An overview for found parameters A and B is presented in Fig. 7. The stronger decrease over angle found with L- and S-band ($B = 2$) is as expected since for longer wavelengths there is less volume scattering from the vegetation canopy and the soil reflections become more dominant. For these longer wavelengths the soil surface roughness appears smoother, causing specular reflection to be stronger and non-specular reflections (including in the backward direction) to decrease more rapidly with θ. This effect is well-known, see for example ?. By the same logic, for X-band σ^0 will decrease more slowly over θ ($B = 2$) as scattering from the vegetation canopy becomes dominant over that from the soil surface. Strong vegetation scattering is known to be more constant over θ (see for example ?) and thus the model for an isotropic scattering surface applies. With C-band both $B = 1$ and $B = 2$ fitted best for about half of the ϕ angles which indicates that at this 'intermediate' wavelength we see both aforementioned features. With the co-polarization channels we see that the average A values over ϕ decreases with increasing wavelength as expected considering the description above. An exception however, is the L-band response with hh polarization which is comparable to that of C-band. As with the asphalt measurements (Appendix 6.1), we believe these high σ^0 retrievals are due to the low angular resolution of our scatterometer for L-band. As a result, the backscatter for close to nadir angles (which are highest in general) is present in all angular positions α_0. This is visible in the inset figure of Fig. G1. We also note that the variation over ϕ (by comparing $S_\phi B_{pp}$ to $\langle B_{pq} \rangle_\phi$) is smallest for X-, and largest for L-band. The cross-response is lower than that for the co-polarization as expected. For both vh and hv the X-band backscatter is also largest here while those for L-band are lowest. However, S-band appears to have stronger backscatter than C-band. We do not have a clear explanation for this. As with the co polarization channels the variation over ϕ is strongest for the longer wavelengths.

Finally some remarks on the variation of A ~~with~~ over ϕ and, virtually, arccos the surface area. Except for X-band with hh polarizations there did not appear to be a systematic trend of A over ϕ. Also, there was not one particular ϕ angle for which the values for A over BW and polarization stood out from the rest. These observations indicate that the surface area covered by our scatterometer appeared to have uniform (scattering) properties. The somewhat higher A values with the negative ϕ values with X-band at hh polarization are probably caused by a difference in vegetation density between the left- and right side of the Maqu site. Fortunately, for $\phi = 0°$ the A value had a medium value compared to the other ϕ angles, so that we may still interpret the surface area associated with the scatterometer's (fixed) footprint during the time-series measurements as being representative for its surroundings.

6.3.1 ~~Time-series σ^0_{pp} Maqu~~

~~Figure 5 presents an overview of the time-series data of σ^0_{pp} over the whole August 2017 − 2018 period for all considered bandwidths in S-, C-, and X-band, along with m_v and T_{soil} at 2.5 and 5 depth. For visibility reasons the graphs only display measurements taken at 18:10 with 2 day intervals. Data of the radar return and σ^0_{pp} for November 2017 is not available, while that of late June − Early July 2018 will become available at a later stage. We observe for all bands and polarizations that σ^0 is highest in summer and autumn while being lowest during winter. This may be explained by the fact that in summer and autumn m_v, and the amount of fresh biomass is high. As a result, the high dielectric constant of moist soil, in combination with the rough surface and presence of water in the vegetation results in strong backscattering. During winter, however, there is little liquid water, i.e. m_v, present in the soil and no fresh biomass (dry biomass however remains present). The dielectric constant of the soil therefore is lower compared to that of moist soil and there is little to no scattering from the dried out vegetation, resulting in a lower σ^0_{pp}. There were however peaks of σ^0_{pp} during winter, for example on 26 January, which coincided with snowfall. Snow cover, deposited on the layer of dead vegetation, forms a rough surface that allows for strong backscatter. The dynamics of σ^0_{pp} during thawing period will be discussed in more detail below.When comparing the three bands we observe that, in general, the backscattering is highest at X-band and lowest at S-band. This difference is caused by the wavelength-dependent response to the surface roughness of the soil and vegetation during the summer and autumn period. For longer wavelengths the soil surface 'appears' more smooth than for the shorter wavelengths, resulting in stronger specular reflection, thus lower backscatter. A similar argument holds for the vegetation; its constituents are small compared to the longer wavelengths, thus little volume scattering occurs.Except for during the summer, backscatter for vv polarization was equal to, or higher than that of hh polarization. This behaviour was also observed by ?, albeit for bare soil. We however may compare our situation to that of bare soil during winter, when there is no fresh biomass. When vegetation was present, σ^0_{hh} was stronger, as is visible during July - August 2018. This was however not the case during August - September 2017, when the vegetation probably still contained water. Somewhat stronger backscatter, 0.5 − 1 , for hh- than for vv polarization was also reported for grassland in ? with $40 \leq \theta \leq 60°$ for S- and X-band. For C-band they reported no clear difference. Yet another study, (?), measured 3-4 dB higher backscatter for hh as for vv for wheat at L-band ($\theta = 40°$).Time-series measurements of σ^0 () for vv and hh polarizations for S-, C- and X-band during 13 days in April 2018. Shaded regions indicate 66% confidence~~
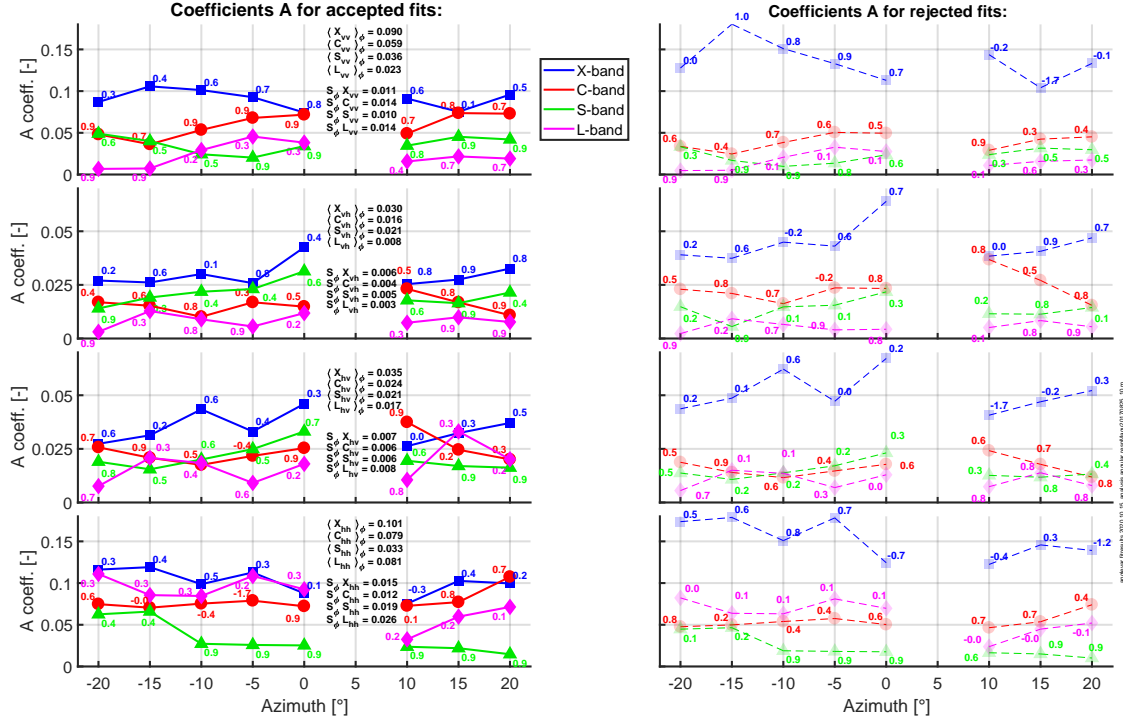
Figure 7. ~~Time-series measurements~~ Results of ~~σ^0 () for vv and hh polarizations for S-, C- and X-band from August 2017~~ fitting the derived values σ_{pq}^0 over α_0 to ~~2018. Shown are measurements taken at 18:10 with 2 day intervals. Shaded regions indicate 66% confidence intervals~~ model $\sigma_0(\theta) = A\cos(\theta)^B$ for σ^0. Antenna boresight angle fixed at $\alpha_0 = 55°$. Range different azimuth angles ~~of incidence are: S-band; $32° \leq \theta \leq 60°$ for vv- and $20° \leq \theta \leq 60°$ for hh~~ϕ, ~~C-band; $34° \leq \theta \leq 60°$ for vv-~~ bandwidths BW, and ~~$39° \leq \theta \leq 61°$~~ polarization channels. Left column shows found coefficients A over ϕ for ~~hh, X-band; $47° \leq \theta \leq 59°$~~ best fits with favourable B-value for ~~vv-~~ each BW and ~~hh~~polarization and right column the A coefficients with less favourable B-values. ~~Bottom graphs show measured volumetric soil moisture content m_v^{5TM}~~ Numbers at data points indicate coefficient of determination (R^2) ~~and soil temperature T_{soil} at 2.5 and 5 depth~~of individual fits. ~~Spatial~~ Values in the centre are average ~~volumetric soil moisture content M_v is estimated~~ $\langle B_{pq} \rangle_\phi$ and standard deviation $S_\phi B_{pq}$ over ϕ, with $B = L, S, C,$ or X as ~~$M_v = m_v^{5TM} \pm 0.04$~~ bandwidth.~~Black arrows indicate rain events, specified by two numbers: rate () × duration ().~~

690 ~~intervals for σ^0. Antenna boresight angle fixed at $\alpha_0 = 55°$. Range angles of incidence are: S-band; $32° \leq \theta \leq 60°$ for vv- and $20° \leq \theta \leq 60°$ for hh, C-band; $34° \leq \theta \leq 60°$ for vv- and $39° \leq \theta \leq 61°$ for hh, X-band; $47° \leq \theta \leq 59°$ for vv- and hh. Bottom graphs show measured volumetric soil moisture content m_v^{5TM} () and soil temperature T_{soil} at 2.5 and 5 depth. Spatial average volumetric soil moisture content M_v is estimated as $M_v = m_v^{5TM} \pm 0.04$. Black arrows indicate rain events, specified~~

by two numbers: rate () × duration (). Figure **??** shows a 13-day period with σ^0_{pp} measured during soil freeze/thaw transitions at 30 minute intervals. In the bottom graph we observe that measurements taken with 5TM sensors at 2.5 and 5 depth. T_{soil} was above 0 during daytime and just below it for some nights. With some days m_v showed diurnal thawing and freezing. The arrows indicate two rain events, with the first it rained 1 for 2 hours and with the second 1 for 10 hours.The most prominent features in the backscatter measurements are the diurnal variations of σ^0_{pp} that are clearly caused by changes of m^v. For all bands and polarizations we observe that σ^0 increases during daytime due to the increase of liquid water in the top soil due to thawing and at night σ^0 drops as most of the water freezes again. With some days, e.g. 3 to 5 April, we observed diurnal changes in σ^0 while the m_v measured by the 5TM sensors showed little variations. This may suggest that the freezing and thawing during those days occurred only in the very top-soil layer, just below the air-soil interface where it was outside the influence zone of the 5TM sensors. The time lag between the drop of σ^0 (first) and the drop of 5TM m_v (second), is caused by the same phenomena as the freezing starts at the top soil layer and progresses downward. The time lag during thawing was smaller.In general the magnitude of the σ^0 -change was largest for X-band and smallest for S-band. This can be explained by the penetration depth. Longer wavelengths penetrate deeper into the soil. As such, should there be radiation scattered back from below the surface then it will have travelled deeper into the soil for S-band than for X-band. As such, the response for X-band will be sensitive to changes in m_v only at the top soil level, while for S-band signatures of change at the top soil layer will be affected by contributions from the deeper layers, in which m_v changes less over time.

Although there are many more interesting features visible only from Fig. **??** alone, a more detailed investigation of the results extend beyond the scope of this paper. Our preliminary analysis demonstrates that the scatterometer data set collected at fixed time-intervals over a full year at the Maqu site contains valuable information on exchange of water and energy at the land-atmosphere interface. Information which is difficult to quantify with in-situ measurements techniques alone. Hence further investigation of this scatterometer data set provides an opportunity to gain new insights in hydro-meteorological processes, such as freezing and thawing, and how these can be monitored with multi-frequency scatterometer observations.

7 Data Availability

In the DANS repository, under the link https://doi.org/10.17026/dans-zc5-skyg the collected scatterometer data is publicly available (**?**). Stored are both the radar-return amplitude and phase for all four linear polarization combinations and processed σ^0 for co-polarization channels (vv & hh). The dataset includes time-series measurements from 26 August 2017 − 26 August 2018, data of angular variation experiment, and radar returns of the reference targets. Accompanying data includes time-series measurements of soil moisture and -temperature profile at depths of 2.5, 5.0, 7.5, 10, ...90, 100 and precipitation measurements.

7 Conclusions

~~In this paper we describe a microwave scatterometer system that~~

A ground-based scatterometer system was installed on an Alpine Meadow over the Tibetan Plateau and ~~its collected dataset consisting of measured radar returns from the ground surface. The observation period was August 2017 – August 2018 and measurements were taken with a one- to half hour temporal resolution. The scatterometer measured the radar return amplitude and -phase over a~~ collected a one-year dataset of microwave backscatter over a broad 1 – 10 GHz band for all four linear polarization combinations.~~The system was build with commercially available components (vector network analyzer, four phase stable coaxial cables, and two broadband dual polarization gain horn antennas) and required little to no maintenance.~~

~~We described a procedure on how to retrieve the co-polarized backscattering coefficients σ^0_{vv} & σ^0_{hh} for a VNA-based scatterometer system with two fixed antennas operating over a broad frequency range (1 – 10). The typical effects resulting from the wide antenna radiation patterns were dealt with by using the narrow-beam approximation in combination with~~ Measurements of the incidence-angle dependence of σ^0_{pq} for asphalt agreed with previous findings, thereby showing our σ^0 retrieval method to be accurate. Presented analysis on the angle-variation data of σ^0 in Maqu showed wavelength- and polarization dependent scattering behaviour due to vegetation that is in accordance with theory and other studies. Furthermore, these measurements indicated the Maqu ground surface to have spatially homogeneous electromagnetic properties and that the area associated with the ~~mapping of function $G^2/R^4(x,y)$ over the ground surface , so that proper footprint positions and -areas, and incidence angle ranges could be derived. The incidence angle range was frequency-dependent and varied from 20 – 65for L-band to 47 – 59for X-band. Since spatial averaging was not possible frequency averaging was applied to reduce fading uncertainty. Bandwidths for averaging were selected with help of the Improved Integral Equation Model (I^{2}EM) for surface scattering.~~

~~Backscatter measurements on a rectangular metal plate reference target were used to calibrate the scatterometer. Verification measurements on the co-polarized radar cross section of a metal dihedral plate showed the calibration to be valid. Measurements~~ of (fixed) footprint for the ~~angle-dependent σ^0_{vv} & σ^0_{hh} of asphalt agreed with previous findings, thus showing our σ^0 retrieval method to be accurate~~time-series measurements to be representative of its surroundings.

The uncertainty of our retrieved σ^0 ~~can be divided in a known part~~consists of quantifiable parts estimated from fading- and systematic measurement ~~uncertainty~~uncertainties, and an unknown part due to ~~low angular resolution of the~~ the low directivity of used antennas. The ~~known measurement~~ quantifiable uncertainty in σ^0 was estimated with an error model providing 66 % confidence intervals that are different over frequency bands, polarizations and the overall level of the radar return. ~~Extreme values for~~Typical $\Delta\sigma^0$ ~~were~~ values during summer range from ± ~~1.3~~1.5 dB for ~~X-band with vv polarization when the overall σ^0 level was highest (during summer) and~~ S-band with hh polarization to ± ~~2.7~~2.5 dB ~~with hh polarizationwhen the overall σ^0 level was lowest (during winter). Despite aforementioned uncertainty~~for L-band with hv polarization. Despite aforementioned uncertainties in σ^0 ~~and the additional unknown uncertainty,~~ we believe that the strength of our approach lies in the capability

of measuring σ^0 dynamics over a broad frequency range, 1 – 10 GHz, with high temporal resolution over a full-year period. ~~On three days during summer the radar backscatter was measured for different angles in elevation and azimuth to quantify the angular dependence of σ^0 and to assess the ground surface homogeneity. Presented~~

Our preliminary analysis on the ~~angle-variation data of σ^0 showed wavelength- and polarization dependent scattering behaviour due to vegetation that is in accordance with theory and previous findings. Furthermore, these measurements indicated that the surface associated with the (fixed) footprint for the time-series measurements to be representative of its surroundings.~~

In the retrieved time-series of σ^0_{vv} & σ^0_{hh} for S-band (2.5 − 3.0), C-band (4.5 − 5.0), retrieved σ^0_{pq} for L-, S-, C-, and X-band ~~(9.0 − 10.0) we observed characteristic changes or features that can be attributed to seasonal changes in the soil. For example a fully frozen top soil, freeze-thaw changes in the top soil, emerging vegetation in spring, and drying of soil.Further studies with obtained dataset allows for in-depth analysis of diurnal changes of surface top-soil moisture dynamics during all periods within the year. Availability of backscattering data for multiple frequency bands allows for studying scattering effects at different depths within the soil and~~ demonstrates that the scatterometer data set collected at fixed time-intervals over a full year at the Maqu site contains valuable information on exchange of water and energy at the land-atmosphere interface, information which is difficult to quantify with in-situ measurements techniques alone. Hence further investigation of this scatterometer data set provides an opportunity to gain new insights in hydro-meteorological processes such as freezing and thawing, or wavelength-dependent scattering effects in the vegetation canopy during ~~the spring~~ spring- and summer periods.~~Finally, combining scatterometer data with measured ELBARA-III radiometry data (?) creates a complementary dataset that allows for in-depth study of the soil moisture and -temperature dynamics below, and at, the air-soil interface.~~

~~The authors would like to express their gratitude towards the European Space Agency (ESA) and Ministry of Science and Technology (MOST) of the P.R. China for funding this research as part of the Dragon 4 cooperation programme.~~

List of Symbols

Symbol	Description	Units
A_{fp}	Surface area of the footprint.	m^2
a	a dimension of reference target frontal projection.	m
α	Angle between tower's vertical axis and the orthogonal projection of the line from antennas to a ground surface segment onto the plane formed by the tower's vertical axis and the antenna boresight direction line. See also Fig. B2. For antenna boresight line $\alpha = \alpha_0$.	°
BW	Bandwidth associated with E_e or σ^0.	GHz
b	b dimension of reference target frontal projection.	m
β	Angle between line from antennas to a ground surface segment and projection of that same line onto the plane formed by the tower's vertical axis and the antenna boresight direction line. See also Fig. B2. For antenna boresight line $\beta = \beta_0$.	°
c	Speed of light.	m s^{-1}
D	Antenna aperture width.	m
~~ΔE_T^g~~ ΔE_T	Temperature-induced radar return uncertainty.	V m^{-1}
ΔI_N	Uncertainty in I_N.	W m^{-2}
ΔK	Reference target measurement uncertainty.	W m^{-2}
E_e	Magnitude of total electric field strength at the receive antenna, originating from the (surface) target.	V m^{-1}
E_e^g	Same as E_e, superscript g denotes ~~Time-domain~~ time-domain filter, or gate, is applied.	V m^{-1}
~~E_n^g~~ E_{cx}^g	~~Noise level of E_e. Superscript~~ Remnant of the transmit-to-receive antenna (direct)cross coupling. This quantity is measured with antennas aimed skywards, superscript g ~~denotes that~~ indicates same time-domain filter, or gate, as ~~used~~ with E_e^g ~~is applied~~was used.	V m^{-1}
~~E_c^{gc}~~ E_b	Lowest measurable signal by scatterometer, or background value of E_e.	V m^{-1}
~~E_0^{g0}~~ E_0^{g0}	Magnitude of total electric field strength at the receive antenna, originating from the reference target. Superscript ~~gc~~ g0 denotes Time-domain filter, or gate, is applied.	V m^{-1}
~~E_{bc}^{gc}~~ E_{b0}^{g0}	Background level of ~~E_c^{gc}.~~ E_0^{g0}. Superscript $g0$ denotes same Time-domain filter, or gate, as with E_0^{g0} is applied.	V m^{-1}
ϵ_0	Permittivity of vacuum (and by approximation that of air).	F m^{-1}
ϵ_{soil}	Effective relative permittivity of a soil, which is a mixture of dry soil, water, minerals, organic material etc. Includes both real and imaginary part component.	−
G	Antenna gain as a function of angle with respect to antenna boresight direction. Maximum value is G_0.	−
H_{ant}	Height of the antenna apertures above the ground.	m

Symbol	Description	Units
I	Time-average intensity of total electric field strength at receive antenna, originating from the (surface) target.	$\mathrm{W\,m^{-2}}$
I_N	Measured intensity averaged over N independent samples.	$\mathrm{W\,m^{-2}}$
$\bar{I}$	The average of a large amount of independent measurements of I originating from a surface with backscattering coefficient σ^0. $\bar{I}$ is a surface property.	$\mathrm{W\,m^{-2}}$
K	Constant (over BW) linking σ^0 to $\bar{I}$	$\mathrm{W\,m^{-2}}$
L	Maximum dimension of target in context of RCS measurement.	m
M_v	Spatial average volumetric top soil moisture ~~content~~ over Maqu site.	$\mathrm{m^3\,m^{-3}}$
m_v	Volumetric soil ~~moisture~~ content.	$\mathrm{m^3\,m^{-3}}$
N	Number of independent scatterometer measurements, or samples, of a (surface)	–
~~NES Noise Equivalent σ^0.~~ P_q^{RX} $\underline{P_p^{Rx}}$	Power received by radar or scatterometer. The subscript refers to the linear polarization direction (horizontal h or vertical v) that is measured by the antenna.	W
P_p^{TX} $\underline{P_p^{Tx}}$	Power transmitted by radar or scatterometer. The subscript refers to the linear polarization direction (horizontal h or vertical v) that is transmitted by the antenna.	W
~~P_q^c~~ $\underline{P_p^0}$	Power received by radar or scatterometer from calibration target. The subscript refers to the linear polarization direction (horizontal h or vertical v) that is measured by the antenna.	W
ϕ	Azimuth, or horizontal rotation angle of antennas.	°
R	Distance antennas to (area) target (segment).	m
R_c	Distance antennas to calibration standard.	m
R_{ff}	Distance from antennas beyond which the antenna far-field radiation region is defined.	m
R_{fp}	Distance antennas to centre of footprint.	m
R_{pw}	Distance from antennas beyond which the wavefront of transmitted radiation is considered planar.	m
r_{sg}	Start of the time-domain filter, also known as gate.	m
r_{eg}	End of the time-domain filter, also known as gate.	m
σ_{pq}	Radar Cross Section (RCS). ~~The first subscript is the~~ First subscript denotes polarization direction (horizontal h or vertical v) of the ~~incident radiation and the second subscript~~ scattered- and second denotes that of the ~~scattered~~ incident radiation.	$\mathrm{m^2}$
σ_{min}	Minimum detectable radar cross section (RCS) by scatterometer given a certain distance to target R.	$\mathrm{m^2}$
σ_{pq}^0	Backscattering coefficient. The ~~first subscript is the~~ radar cross section (RCS) associated with a distributed target over a certain (physical) area. First subscript denotes polarization direction (horizontal h or vertical v) of the ~~incident radiation and the second subscript~~ scattered- and second denotes that of the ~~scattered~~ incident radiation.	(–)

Appendix A: ~~Derivation spatial soil-moisture-variation estimate~~Results supporting measurements

 A1   Photographs site phenology

In this section we present a set of photographs of the Maqu site taken at different seasons since the installation of the ELABRA-III in January 2016. These may give the reader a global indication of how the site phenology changes throughout the seasons.
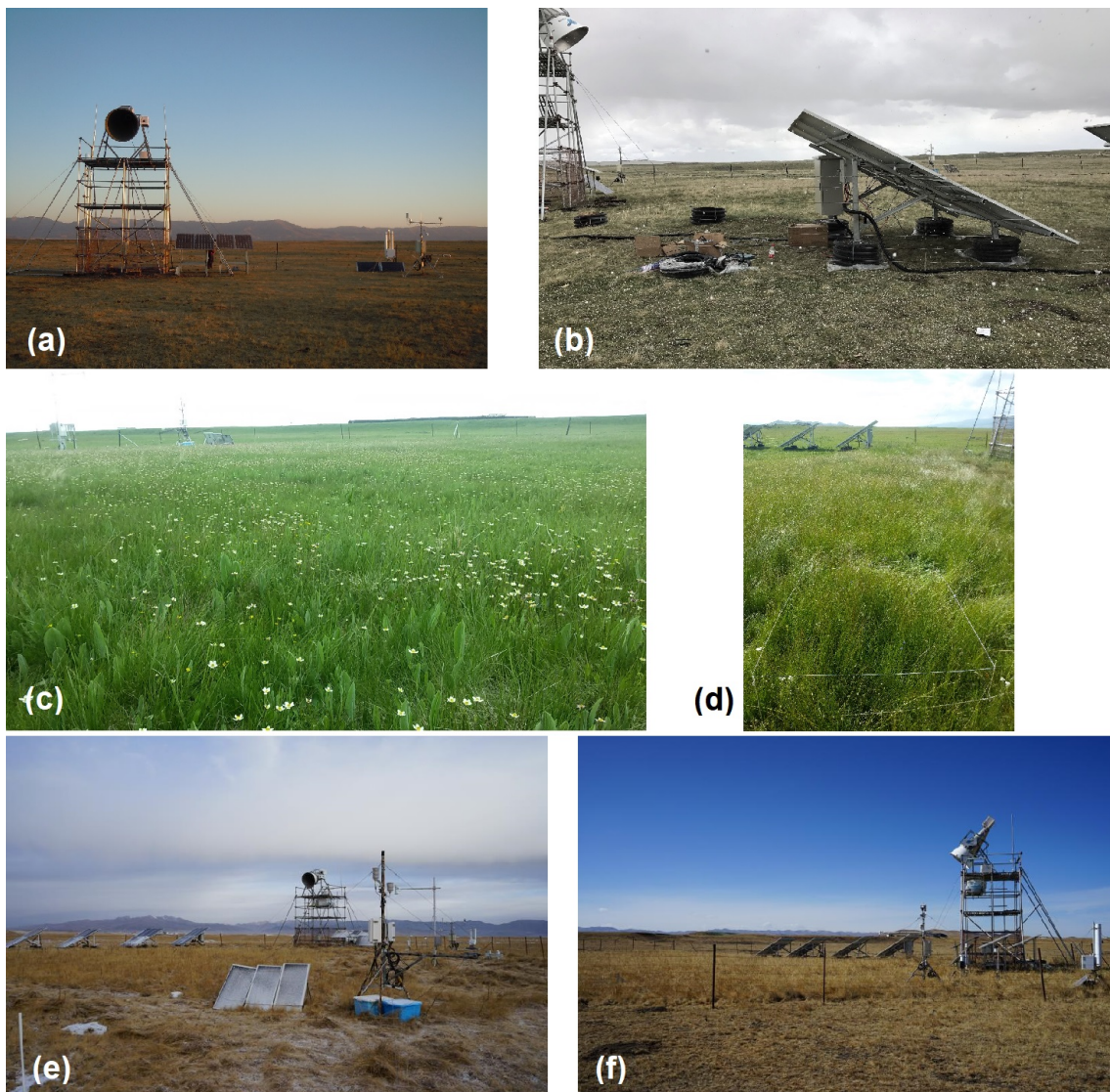
Figure A1. Maqu site changing phenology. (a) Winter, January 2016. (b) Spring, 16 May 2017. (c) Spring, 26 June 2018. (d) Summer, 17 August 2018. (e) Winter, 6 January 2018. (f) Winter, 6 January 2018.

A2 Hydrometeorological sensors and -measurement results

Table A1 lists all hydrometeorological instruments used for this study along with their reported measurement uncertainties. Air temperature was measured with a Platinum resistance thermometer, type HPM 45C, installed 1.5 m above the ground and precipitation (both rain and snow) was measured with a weight-based rain gauge, type T-200B.

We formulate in brief our main observations over the measured hydrometeorological quantities at the Maqu site over the period

Table A1. Overview of relevant hydrometeorological sensors Maqu site

Quantity	Type, Manufacturer:	Unit, Uncertainty:
Volumetric soil moisture m_v	5TM, Meter Group	± 0.02 $\mathrm{m^3\,m^{-3}}$ (?)
Volumetric soil moisture m_v	ThetaProbe ML2x, Delta-T Devices	± 0.05 $\mathrm{m^3\,m^{-3}}$
Soil temperature	5TM, Meter Group	± 1 $^\circ$C
Air temperature	HPM 45C, Campbell Scientific	± 1 $^\circ$C
Precipitation (rain & snow)	T-200B, Geonor	± 0.6 mm
Short- and long wave up- and downward irradiance	NR01, Hukseflux	$\pm 5\%$ $\mathrm{W\,m^{-2}}$

26 August 2017 – 26 August 2018. Figure A2 provides an overview with a two-day temporal resolution. All data are available in the dataset with a temporal resolution of 30 minutes.

The lowest air temperatures T_{air} were measured in January 2018, during which daily minimum values dropped below -20 $^\circ$C while daily maximum temperatures did not rise above 0 $^\circ$C. In July – August 2018 T_{air} was highest with maxima above 20 $^\circ$C.

Soil temperature T_{soil} and soil volumetric liquid water content m_v varied over depth. Depending on the amount of liquid water in the soil, the penetration depth of frozen soil at L-band can vary from 10 – 30 cm at the Maqu site (?). We consider T_{soil} and m_v values at 25 cm depth, which is closest to the maximum aforementioned penetration depth. From the measurements we conclude that at 25 cm depth the soil can be considered frozen between 21 December 2017 – 5 April 2018 (arrows in figure). For other depths the freezing- and thawing process is substantially different from the shown curves. During the 2017 – 2018 winter T_{soil} dropped below 0 $^\circ$C up to a depth of 70 cm (not shown in Fig.A2).

Total precipitation over the considered one-year period was 688 mm. The majority of this amount fell in the months September, October 2017 and in August 2018, while from November 2017 to the middle of March 2018 there was only 7 mm precipitation. Presence of snow on soil was inferred from the observed noon albedo to be 0.4 or higher.
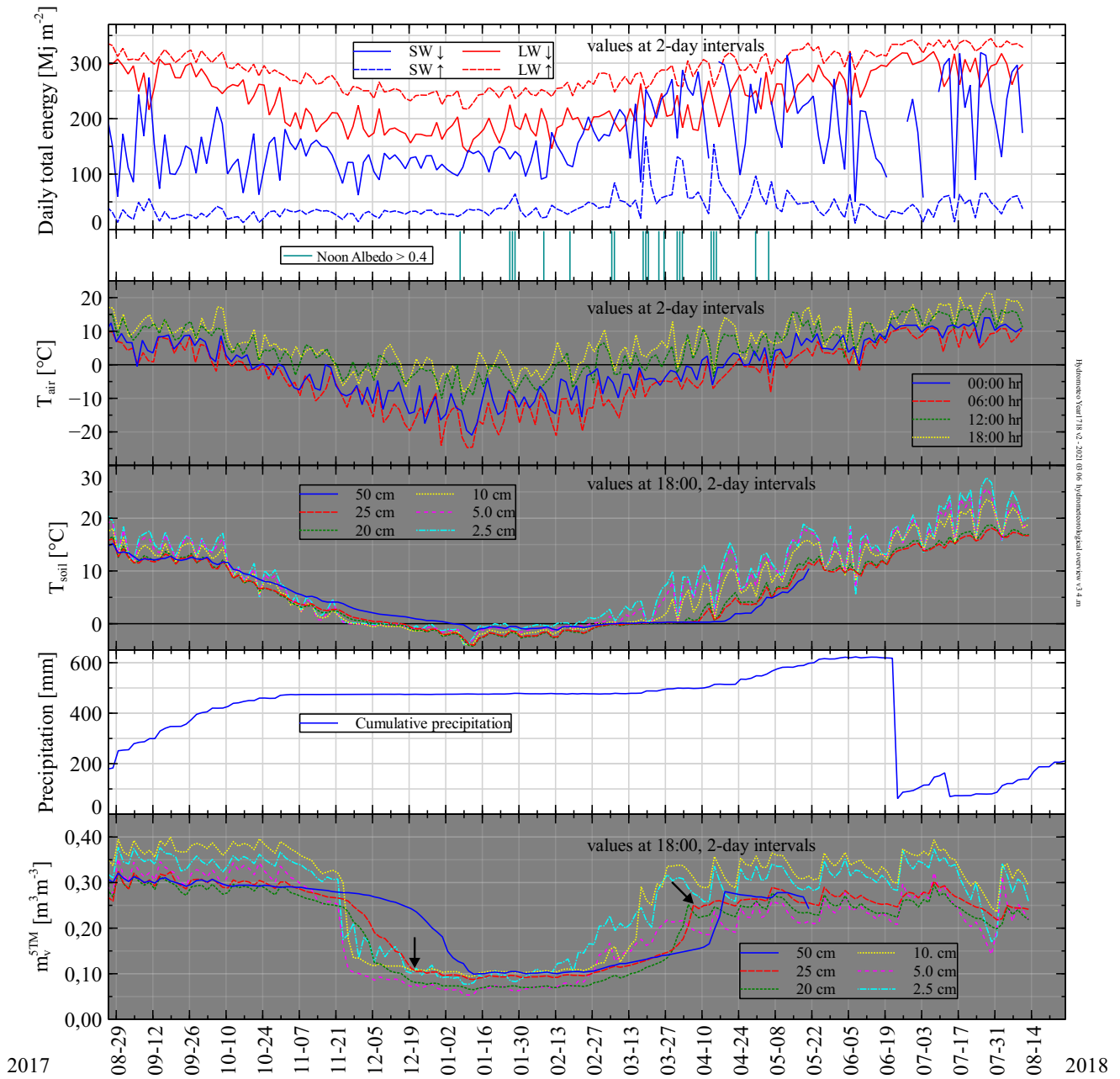
Figure A2. Overview of hydrometeorological quantities measured at Maqu site over period 26 August 2017 – 26 August 2018. From top to bottom: Daily total sum of down- and upward hemispherical energy $(\mathrm{Mj\,m^{-2}})$ for short- (285 - 3000 nm) and long (4500 - 40000 nm) wavelengths at two-day intervals, days with snowfall (identified from noon albedo), air temperatures $(^\circ\mathrm{C})$ at four times during the day at two-day intervals, soil temperatures T_{soil} $(^\circ\mathrm{C})$ for different depths at two-day intervals, cumulative precipitation mm, and volumetric soil moisture m_v^{5TM} $\mathrm{m^3\,m^{-3}}$ for different depths at two-day intervals. Arrows indicate freeze/thaw of soil at 25 cm. Spatial average volumetric soil moisture M_v is estimated as $M_v = m_v^{5TM} \pm 0.04$ $\mathrm{m^3\,m^{-3}}$.

A3   Derivation spatial soil-moisture-variation estimate

This section describes how the spatial average soil moisture content over the Maqu site M_v (m^3 m^{-3}) is linked to m_v as measured by the 5TM sensors at 2.5 and 5 cm depth.

At every depth, m_v varies over the horizontal spatial extent at all scales (?). Local m_v variability is caused by variations in soil structure and texture, including organic matter. At the Maqu site, the 5TM sensor array forms only one spatial measurement point for soil moisture. We denote its measurements as m_v^{5TM} (m^3 m^{-3}). In an attempt to quantify how m_v^{5TM} at the top soil layer (depths 2.5 and 5 cm) relates to the soil moisture over the rest of the Maqu site, we sampled m_v at 17 positions along the no-step zone (Fig. 2) on June 29th 2018 with a hand held impedance probe, type ThetaProbe ML2x, whereby 3 measurements were taken per position. Figure A3 shows the measured m_v in the top layer. Taking aside the outlying values at positions 1 and
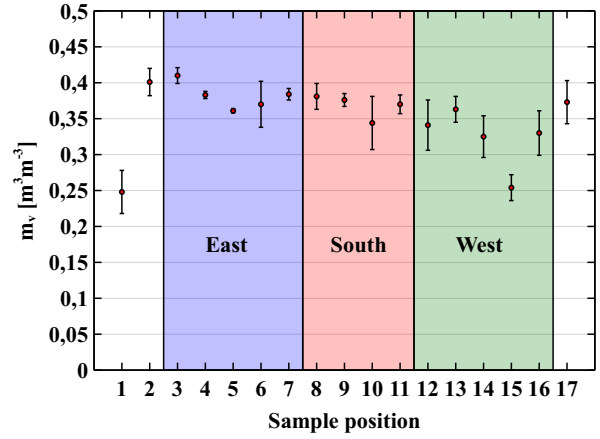
Figure A3. Top-soil m_v measured with hand-held ThetaProbe at 17 sample positions along no-step zone periphery (indicated Fig. 2). Vertical bars denote minimum and maximum values of the 3 measurements per sample position. Red dots represent median values.

15, we observe that the trend along the periphery is slightly larger than the variability amongst the three measurements taken at a specific position. The average standard deviation over the 15 positions is 0.03 m^3 m^{-3} while the average standard deviation over the three measurements is 0.02 m^3 m^{-3}. Given this small difference we concluded there is no clear trend of top soil m_v at the Maqu site. Therefore, we considered all $15 \times 3 = 45$ readings as independent measurements on spatial m_v variation, that we used to create the quantity S_t (S_{tot} (m^3 m^{-3}), called the total standard deviation of spatially measured m_v, which is an estimate for the spatial m_v variability over the Maqu site. Subsequently, we use S_t S_{tot} to relate the measured m_v^{5TM} to the spatial average top soil moisture content over the Maqu site M_v (m^3 m^{-3}) according to

$$M_v = m_v^{5TM} \pm S_{tot} \tag{A1}$$

Using the assumption of temporal stability of spatial heterogeneity (?) we consider found S_t S_{tot} to hold throughout the year. S_t S_{tot} is calculated by

$$S_t = \sqrt{S_s^2 + S_{5TM}^2 + S_p^2} \tag{A2}$$

according to standard error propagation theory (see for example ?). The term S_s ($m^3\,m^{-3}$) represents the spatial m_v variability as measured along the periphery. It is calculated as the standard deviation over $45-1$ samples and is 0.031 $m^3\,m^{-3}$. The standard deviation S_{5TM} a has value of 0.02 ($m^3\,m^{-3}$) and is the root-mean-square measurement error of the 5TM sensors. It was derived in ? after calibrating 5TM sensor retrievals to top-soil gravimetric soil samples taken at the Maqu site. The term S_p is the propagated error of the 0.05 $m^3\,m^{-3}$ theta probe measurement accuracy (Table A1) when S_s is calculated. $S_p = 0.05/\sqrt{45-1} = 0.0075$ $m^3\,m^{-3}$. Finally, S_t S_{tot} then is 0.04 $m^3\,m^{-3}$.

A4 Vegetation sampling

Table A2. Measured vegetation parameters at Maqu-site during summer 2018

	12 July 2018	17 August 2018
Height (distribution max.) (cm)	25	40
Biomass Fresh ($Kg\,m^{-2}$)	0.9	1.3
Biomass Dry ($Kg\,m^{-2}$)	0.3	0.5
VWC (%)	60	62
LAI ($m^2\,m^{-2}$)	3.5	7

Appendix B: ~~Details~~ Technical details scatterometer calibration

B1 ~~Measurement of reference targets~~ Connection scheme and VNA operation

In Fig. B1 the used connection scheme is shown. The front-panel jumpers were removed and the two dual polarization broad band horn antennas were directly connected to the VNA's sources and receivers via the four coaxial cables. This configuration allows for measuring all four polarization channels: vv (i.e. receive in vertical direction, transmit in vertical direction), vh, vh, and hh (?). Between all four coaxial cables and their respective VNA connectors 10 dB attenuators, type SMA attenuator R411.810.121 (manufacturer: Radiall) were inserted to prevent interference from internal reflections travelling multiple times up- and down the coaxial cables.

Measurements were performed by instructing the VNA to measure the four scattering parameters (S-parameters)[1] ($-$) over a stepped frequency sweep $0.75-10.25$ GHz. Given the aforementioned connection scheme the correspondence between recorded S-parameters and transmit- /receive polarization channels are as indicated in Fig. B1b. Used connection configuration

---

[1]Not to be confused with the scattering amplitudes used in scattering theory, which have units m, see for example ?.
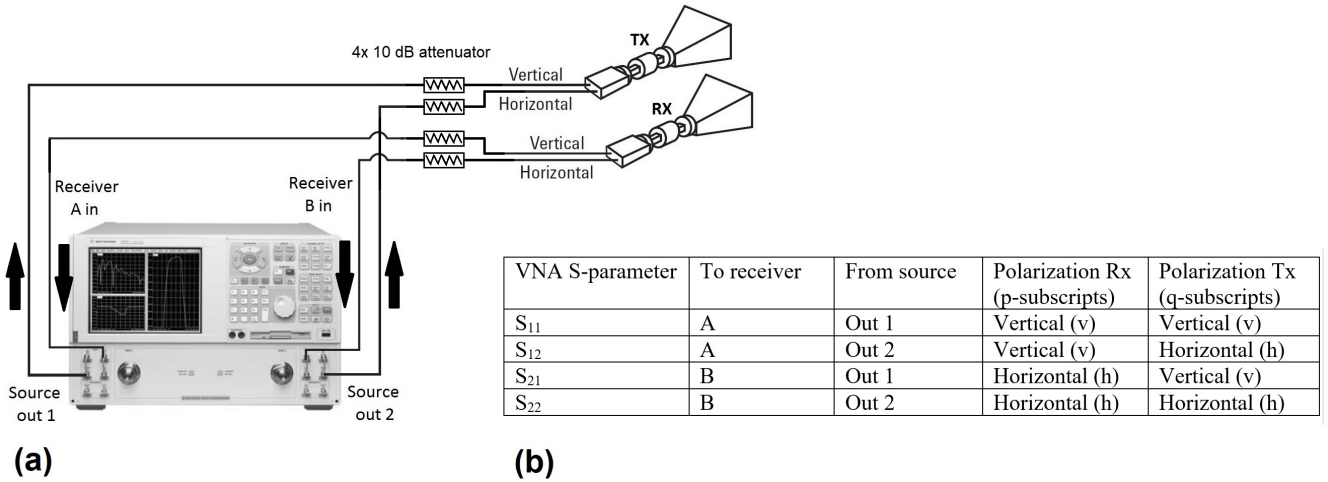
Figure B1. Connection scheme of scatterometer and correspondence S-parameters to polarization channels for transmit (Tx) and receive (Rx). (a) Both dual polarization broadband antennas, one for Tx, the other for Rx, are connected to the VNA as indicated (**?**). Arrows indicate direction of signal. (b) Overview correspondence of four VNA S-parameters to the four polarization channels.

omits the VNA's internal test-port couplers which are typically used when measuring (two-port) S-parameters. The VNA software -by default- accounts for these test-port couplers by adding 16 dB to the signal measured by receivers A and B when calculating the S-parameters. With the σ^0 retrieval this 16 dB 'amplification' cancels out as the target- is divided by the reference return. However, when considering the received powers individually, as done in Sec. 6.2, this factor should be considered.

B2 Geometries of experimental setup

Figure B2(a) shows all relevant geometries for the performed experiments. The two antenna apertures are at distance H_{ant} above the ground surface. The separation between the two antenna apertures $W_{ant} = 0.4$ m is small compared to the target distance (ground or calibration standards) which justifies using the geometric centre of the two apertures for all calculations. Every area segment dA (m^2) of the ground surface has its own distance to the antennas R and angle of incidence θ. Angles α and β are angular coordinates of R. Angle α is defined between the tower's vertical axis and the orthogonal projection of the line from antennas to a ground surface segment onto the plane formed by the tower's vertical axis and the antenna boresight direction line. Angle β is defined between line from antennas to a ground surface segment and projection of that same line onto the plane formed by the tower's vertical axis and the antenna boresight direction line. The planes in which α and β lie are also the antenna's principal planes (see for example (**?**)). For the antenna boresight direction $\alpha = \alpha_0$ and $\beta = \beta_0$. The antenna rotation around the tower's vertical axis is defined as azimuth rotation ϕ. The green ring on the ground surface in Fig. B2(a) is related to the time-domain gating process described further on in Sec. B1.

According to **?** the antenna's far field distances R_{ff} (m) are linked to the antenna's largest aperture dimension D (m) and
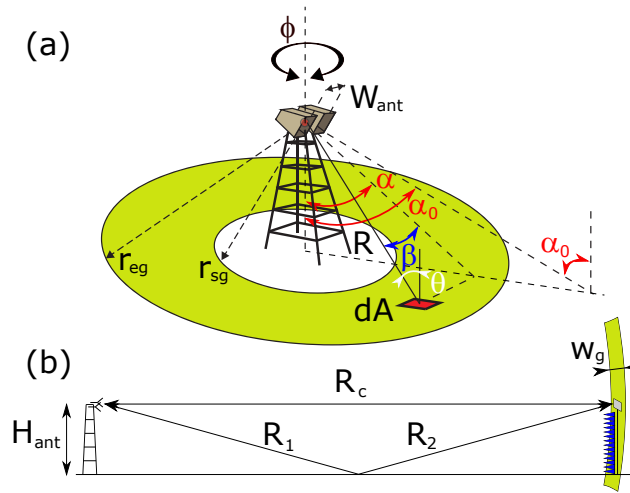
Figure B2. Schematic of scatterometer geometry. (a) Every infinitesimal area dA has its own distance R to the geometric centre between antenna apertures (red dot) and angle of incidence θ. Angles α and β lie within the antennas principal planes, α_0 denotes the angle of antenna boresight. The green ring is a projection of the spherical gating shell with radii r_{sg} and r_{eg} onto the ground. (b) Side view of geometry during measurement of reference standards. Green ring depicts cross section of spherical gating shell with width w_g.

860 wavelength λ via

$$R_{ff} \geq \begin{cases} 5D & : \frac{1}{3} \leq \frac{D}{\lambda} \leq \frac{5}{2} \\ \frac{2D^2}{\lambda} & : \frac{5}{2} < \frac{D}{\lambda} \end{cases} \tag{B1}$$

The antenna aperture is rectangular with dimension $D = 0.2$ m, which leads to $R_{ff} \geq 1$ m for 1 - 3.5 GHz and $R_{ff} \geq 2.7$ m for 3.5 - 10 GHz. Given that with all measurements the distance to the ground surface is larger than 2.7 m the radiation patterns as measured by the manufacturer apply, see Fig. B3 (**?**).

865

Figure B2(b) show a side view of the setup when radar returns of the reference targets were measured in order to calibrate the scatterometer. The reference targets: a rectangular metal plate and two metal dihedral reflectors, were placed at distances R_0 from the antennas on top of a metal mast. To shield this mast pyramidal absorbers were placed in front of it as shown. Next section describes the calibration process in detail.

870 **B3   Calibration**

We measured the radar returns of reference targets with known radar cross section (RCS) σ_{pq} in order to calibrate the scatterometer. ~~A~~ For the co-polarization channels a rectangular metal plate was used as reference target~~for the co-polarization channels . Next, as verification of the calibration process we measured σ_{pp} of~~. As a depolarizing reference target for the cross-polarization channels we used a metal dihedral reflector that was rotated 45° around the axis perpendicular to the vertex
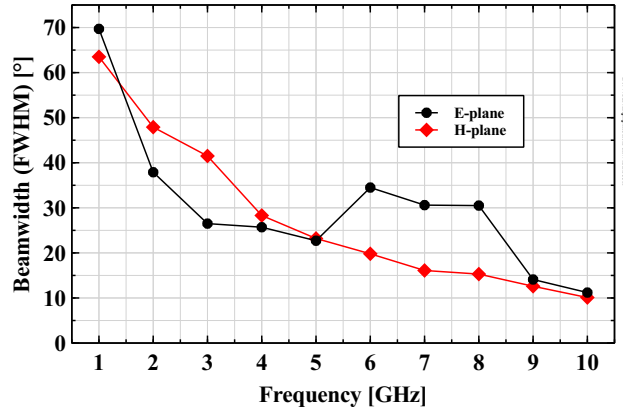
Figure B3. Beamwidths of dual polarization antennas. Shown is the full width half maximum (FWHM) of the measured radiation intensity patterns in the two principal planes (**?**).

connecting the dihedral's two faces and contained in the symmetry plane also holding the same vertex. The physical optics model used for calculating the RCS of a metal plate and dihedral reflector is

$$\sigma_{pp} = 4\pi \frac{(ab)^2}{\lambda^2} \tag{B2}$$

where a and b are the standards' dimensions (m) in the frontal projection (**?**). As is shown in for example (**?**), Eq. B2 is also applicable for calculating the cross polarization RCS of the dihedral reflector when in its rotated position.

There are validity conditions for model B2 which concern the reference target's size and the distance at which it is measured $R_c R_0$. Additionally, ~~R_c should be picked such to prevent interferences from ground reflections.~~ the multi-path field illumination of the reference targets (**?**) might be an issue: besides direct illumination from the transmit antenna, radiation reflected from the ground will also illuminate the target, see Fig. B2(b). As a result, the direct signal is interfered by these ground-to-target reflections. Table B1 lists the used R_c values for the deployed reference standards. We first describe the validity conditions for model B2.

Conditions for Eq. (B2) are that the standard's largest dimension L (m) is large compared to the wavelength, i.e. $L > \lambda$, and

Table B1. Deployed reference standards and their bandwidths of validity

	Distance ~~R_c~~ R_0:	PW -criteria met for:	$L/\lambda \geq 3$ for:
Large rectangular plate, a = 85 cm, b = 65 cm	36.3 m	$f \leq 7.5$ GHz	$f \geq 1.5$ GHz
Small dihedral reflector, a = 57 cm, b = 38 cm	27.7 m	$f \leq 13$ GHz	$f \geq 2.4$ GHz
Large dihedral reflector, a = 120 cm, b = 65 cm	27.7 m	$f \leq 3$ GHz	$f \geq 1.4$ GHz

that the incident wavefront is close to planar. **?** proposed the following equation for calculating the minimum distance R_{pw} (m)

beyond which the wavefront can be considered planar (allowing for a $\pi/8$ phase error):

$$R_{pw} = \frac{2L^2}{\lambda} \tag{B3}$$

890   Concerning the condition $L > \lambda$, previous measurements (**?**) showed, empirically, that for $L/\lambda \geq 3$ model (B2) matches a standard's measured σ_{pp} within 1 dB. Besides used ~~R_c~~ R_0 values, Table B1 also lists the frequency ranges for which the plane wave criteria (using the stated values ~~R_c~~ R_0) and the size criteria hold. ~~The~~ Strictly speaking, the plane-wave criteria with the rectangular plate was not met for 7.5 - 10 GHz. Yet, the co-polarization σ measurement of the ~~verification measurement of~~ ~~σ_{pp} for the~~ small dihedral reflector~~(see Sec. **??**) showed satisfactorily resemblance with the model B2 values, indicating that~~

895   ~~the calibration (using the large rectangular plate) was correct~~ , discussed in Sec. E3.1, yields results close to the Eq. B2 value, indicating correct values for 7.5 – 10 GHz.

~~Now we describe the ground interference issue . Figure B2(b)depicts two pathways for the scatterometer signal to travel to the calibration standard and back. We wish to only measure the response travelling via the direct pathway, $2 \times R_c$. Any contributions from alternative pathways that travel via ground reflections, as shown in the figure, are undesirable since these~~

900   ~~could interfere with the direct path response. Undesired ground reflections can be removed during post-processing via time-domain filtering, or gating (see Sec. **??** and Appendix **??**), provided the difference in total travel time, or distance,~~

Now we discuss the possible issue of multi-path illumination by ground-to-target reflections (GTR's). Should the signal strength of these GTR's be significant, the magnitude-over-frequency response of the reference targets will exhibit interference ripples, which complicate interpreting their radar return for the purpose of calibrating the scatterometer. By using gating the

905   GTR's could in principle be removed from the direct target response, provided their difference in geometrical path length is large enough ~~. Naturally, with greater R_c the difference $R_c - (R_1 + R_2)$ will become smaller. We used a minimum distance of 1.1 , which follows from the sum of the used gate width for the calibration target $\tau_g = 1.7$, which is equivalent to $w_g = 0.5$ plus the widest used pulsewidth resulting from the narrowest used frequency bandwidth BW of 0.5 (Sec. C2): $\tau_p = 1/BW = 2$, which is equivalent to $c\tau_p = 0.6$. The ground reflection~~ for placing a gating window solely over the direct path reflection in

910   time domain. The GTR path shown in Fig. B2(b) was the pathway whose ~~distance~~ path length was closest to that of the direct route. ~~Since the difference between $2R_c$ and $R_1 + R_2 + R_c$ was 1.35 (< 1.1) we were able to filter this out. The metal fence of the Maqu site posed another potential source of interference, but because it was separated from the calibration standards by at least 4 its contribution was easily filtered out with the employed gating filter.~~

B4   ~~Results calibration validation~~

915   ~~Figure E2 shows the measured radar returns $E_c^{gc}(f)$ of the three calibration standards, whose shapes over frequency are explained as follows. With all returns there is a sharp trough between $8 - 9$, which is caused by a combination of a local increment of the antenna's return loss and an asymmetry in the antennas E-plane radiation pattern between $7 - 9$. The asymmetry causes the pattern's peak to point off-target by about $10°$ resulting in a lower radar return. The deep troughs close to 1.3 are caused by a combination of high return loss at the low-frequency edge of the antenna's operational bandwidth and an~~

920   ~~artefact of the gating procedure, which in this case lets $E_c^{gc}(f)$ rise at the edge. This gating artefact is known to distort the band~~

edges of a gated frequency response (**?**). To account for this artefact the bandwidths used for the ground surface measurements were broadened by 10% at both edges prior to gating.The added edges were discarded again after gating. Measured radar returns of calibration standards for co polarization E_c^{gc}. Solid lines are VV- and dotted lines are HH polarization. The curves of the rectangular plate and small dihedral reflector have a similar shape for most of the frequency band. Their difference is merely a constant factor as predicted by the physical optics model for RCS (Eq. B2). The curve shape of the large dihedral reflector however is clearly different from the other two because the planar-wave condition, necessary for model B2, is not met for most of the frequency band, see Table B1.Also, this GRT path will have the strongest coherent ground reflection since it is specular. Naturally, with smaller R_0 the difference $R_0 - (R_1 + R_2)$ increases, allowing one to better distinguish this GRT from the mean reflection.

Measured RCS values of small and large dihedral reflectors as verification of Co-pol scatterometer calibration. Red curves are RCS of small dihedral reflector, green curves that of large dihedral reflector. Solid lines are VV- and dotted lines HH polarization. Solid black lines represent theoretical physical optics model of the RCS. The dotted lines above and below are 1 dB deviation lines shown here as guide to the eye. The radar return of the large rectangular plate was used to calibrate the scatterometer for co-polarization. To validate the calibration we derived the RCS of both dihedral reflectors. As is shown in Fig. **??**, the RCS of the small dihedral reflector matches the physical optics model satisfactorily from $4 - 10$ However, no (clear) presence of any GRT could be found. Using a $BW = 0.5$ GHz . The local peak between $8 - 9$ is caused by aforementioned radiation pattern asymmetry that causes any minor misalignments between the two standards, i.e. antennas with respect to the rectangular plate vs. antennas with respect to dihedral reflector, to result in erroneous RCS values. Furthermore, with hh polarization the rectangular-plate return (Fig. E2) was close to noise level at 8.4 resulting in division by a very small number when calculating the RCS. Below 2.5 the retrieved RCS starts deviating from the theoretical curve because the standard's dimensions become too small compared to the wavelength. Note that 2.5 GHz is close to the value listed in Table B1 based on the empirical requirement $L/\lambda \geq 3$. The measured RCS of the large dihedral reflector is lower than the theoretical curve above 4 because its distance R_c is too small to satisfy the planar-wave condition. Between $1.5 - 3$ the retrieved RCS is still about 1 lower compared to that of the model value. However, the measured curve's slope matches that of the theoretical curve satisfactorily, better in fact than that of the small dihedral reflector over the same frequency range. The reason being that the criteria $L > \lambda$ is clearly met for the large dihedral reflector.bandwidth leads to a $\tau_p = 1/BW = 2$ ns resolution in the time-domain, which would allow us to see the shortest GTR-path reflection that -if present- should be at $[2R_c - (R_1 + R_2 + R_c)]/c = 5$ ns behind the direct-reflection peak. But even with S-band for hh-polarization (broad antenna pattern and for hh-polarization the coherent ground reflection is strongest) no GRT reflections could be found.

We conclude that by using the rectangular plate as reference target for calibrating the scatterometer, measured σ_{pp}^0 values are accurate between $1.5 - 10$ with an offset of approximately -1 for $1.5 - 3$ Because we could not find evidence of GRT interference we hypothesize that the GRT's were too small in magnitude for our case. The antenna patterns, certainly for the lower frequencies are broad enough to illuminate a large part of the ground surface, but because of the dense grass cover

the coherent forward reflections were probably low. Additionally the bistatic RCS patterns of both the rectangular plate- and dihedral reflector are too narrow, even with L-band, for a sufficient amount of energy to be reflected (in a specular manner) back to the receive antenna. Typically the presence of interference due to multi-path illumination with setups like ours is tested by moving the reference target horizontally over a distance of half a wavelength and observing any changes in the signal. Unfortunately this procedure was not possible with our equipment.

Appendix C: ~~Gating~~

B1 Gating

For simplicity, instead of using the (complex) electric field strength measured at the scatterometer's receive antenna E_e, we explain the gating process with the term X (V), which can be considered proportional to E_e by some scatterometer system constant. The measured frequency-domain signal $X[\omega_h]$ was transformed into the time-domain via the Inverse Digital Fourier Transform (IDFT), see for example (?)

$$x[t_n] = \sum_{h=1}^{N} X[\omega_h] e^{i\omega_h t_n} \tag{B1}$$

N is the total number of discrete frequency points within the bandwidth BW (Hz) considered. Angular-frequency points ω_h ($\mathrm{rad\,s^{-1}}$) and time points t_n (s) are calculated with the minimum- and maximum frequency of BW, f_{lo} and f_{hi} respectively (Hz) via

$$\omega_h = 2\pi \left\{ [h-1] \left(\frac{f_{hi} - f_{lo}}{N-1} \right) + f_{lo} \right\} \qquad h = 1, 2, 3, ..., N \tag{B2}$$

$$t_n = \frac{n-1}{f_{hi} - f_{lo}} \qquad n = 1, 2, 3, ..., N \tag{B3}$$

Next the time-domain response $x[t_n]$ was multiplied by the time-domain filter, or gate, which was a block function of width τ_g whose sides ~~fall~~ fell off according to a rapidly decaying Gaussian function, zeroing all signal not coinciding with the unity values. The gate's start- and end times corresponded to the distances indicated in Fig. B2(a): $t_{sg} = 2r_{sg}/c$ and $t_{eg} = 2r_{eg}/c$ respectively~~. In this manner~~, so in effect, only the surface's scattering events of interest remained in the signal. Graphically, this ~~is the intersection of depicted green ring of Fig. B2~~ process is displayed in Fig. B2(a). When assuming isotropic radiating and receiving antennas, selecting a certain time gate is equivalent to only considering scattering 'events' within a spherical shell, centred at the antennas, with radii r_{sg} and r_{eg}. The intersection of said shell with the ground surface then is a ring as shown in the figure. However, our actual antennas have non-isotropic radiation patterns. So it are in fact the surface scattering events associated with the area formed by the intersection of shown green ring and the scatterometer footprint A_{fp} ~~. The~~ that are contained in the signal. As the next step, the gated signal $x[t_n]$ was ~~then~~ transformed back into the frequency domain via the Digital Fourier Transform (DFT)

$$X[\omega_h] = \frac{1}{N} \sum_{n=1}^{N} x[t_n] e^{-i\omega_h t_n} \tag{B4}$$

985   which then contains only the surface scattering information.

    The frequency dependence of the radiation patterns, as shown in Fig. B3, complicates the process described above. The time-domain equivalent of the transmitted scatterometer signal is a pulse of width $\tau_p = 1/BW$ s. Depending on the angle with respect to boresight, i~~,e, .~~.e. α & β, this signal pulse will contain different frequencies, and will therefore have a different

990 temporal shape. At greater angles α & β, high-frequency components of the pulse are not present causing the pulse to be broader there. As a result, the footprint area A_{fp}, which is determined from the (known) antenna radiation- or gain patterns G and the gate width $w_g = c\tau_g$ will become broader. ~~By~~ We avoided this issue by narrowing our bandwidths such that the radiation patterns of the frequencies within can be considered equal~~we avoided this issue. For the lower frequencies~~. As a consequence, this meant that for lower frequencies the selected BW ~~should be narrower~~ had to be more than those for the

995 higher frequencies. Used bandwidths were ~~$BW = 0.5$~~ 1.5 – 1.75 GHz for L-band, 2.5 – 3.0 GHz ~~, $BW = 0.5$~~ for S-band, for 4.5 – 5.0 GHz ~~and $BW = 1$ for~~ for C-band, for 9 – 10 GHz for X-band. Note that there were additional considerations for picking these BW values, which are explained in Sec. C2.

  ~~However, when~~ When measuring the reference target backscatter ~~response E_c ()~~ responses E_0 (V m^{-1}) however, the full 0.75 – 10.25 GHz frequency range can be used. Because the solid angle extending the standard is small we may reasonably assume

1000 that all frequencies are present in the time-domain equivalent pulse at the standard, i.e. $G(\alpha,\beta) \approx 1$ for all frequencies. The benefit of using this broad bandwidth (9.5 GHz) is a high temporal/spatial resolution in the time domain, which allows for precise placement of the gate over the reference target response.

Appendix C: Technical details σ^0 retrieval procedure

C1   Implementation of the radar equation

1005 We rewrite Eq. 3 so that the backscattering coefficient of the surface σ^0 (m^2 m^{-2}) is related to the average received backscattered intensity $\bar{I}$ (Wm^{-1}) as (?)

$$\sigma^0 = K^{-1}\bar{I} \tag{C1}$$

where for brevity the polarization subscripts are omitted. The factor K (W m^{-1}) is a constant for the bandwidth considered given by

1010
$$K = \frac{\lambda^2}{4\pi^3} I^t \frac{G^2}{R_{fp}^4} A_{fp} \tag{C2}$$

where I^t (W m^{-2}) is the transmitted intensity by the scatterometer. For all terms in K the centre frequency is used. Similar as with Eq. 2, we can substitute I^t in Eq. C2 by the relevant radar parameters when a reference target is measured, yielding

$$K = \frac{1}{2}c\epsilon_0(E_0^{g0} - E_{b0}^{g0} - E_b)^2 \frac{G(\alpha,\beta)^2}{G(\alpha_0,\beta_0)^2} \left(\frac{R_0}{R_{fp}}\right)^4 \frac{A_{fp}}{\sigma} = \frac{1}{2}c\epsilon_0(E_0^{g0} - E_{b0}^{g0} - E_b)^2 \left(\frac{R_0}{R_{fp}}\right)^4 \frac{A_{fp}}{\sigma} \tag{C3}$$

E_0^{g0} (V m^{-1}) is the measured backscattered field from the reference target (subscript 0 represents 'reference') and E_{b0}^{g0} (V m^{-1}) is the measured background level during calibration, i.e. the measured backscattered electric field when the calibration standard was removed from the mast while the pyramid absorbers remained in place. With both terms the superscript $g0$ (for 'gate' during reference measurements) indicates that an identical gate was used. The field strength associated with the minimum signal level measurable with the scatterometer is denoted E_b. The prefactors light speed c (m s^{-1}) and the permittivity of vacuum ϵ_0 (F m^{-1} m^{-1}) convert the electric field strengths into time-average intensity. In the middle part of Eq. C3 the antenna gain functions are written explicitly. $G(\alpha, \beta)$ represents the antenna gain functions when measuring the ground return, while $G(\alpha_0, \beta_0)$ represents the situation when the radar return of the reference targets is measured. When using the narrow beam approximation (Eq. 3) and when the reference target is aligned to the antenna boresight direction the fraction becomes unity and the right part of Eq. C3 follows. The middle part is used in Appendix. E3.1 when alignment uncertainty of the reference targets is discussed.

In the context of Rayleigh fading statistics with square-law detection (?), the average received intensity $\bar{I}$ (W m^{-2}) is linked to I_N (W m^{-2}), which is the measured intensity averaged over N independent samples (N footprints or N frequencies), according to

$$\bar{I} = \frac{I_N}{1 \pm 1/\sqrt{N}} \tag{C4}$$

Note that $\bar{I}$, like σ^0 is an implied ground surface property. The quantity that is actually measured, I_N, is an estimator for $\bar{I}$. Equation C4 holds for $N \geq 10$, since then the probability density function of I_N approaches a Gaussian distribution (?) according to the central limit theorem. The denominator in Eq. C4 represents a 68% confidence interval (± 1 standard deviation) for $\bar{I}$. More details on fading are described next in Sec. C2.

In turn, I_N is calculated from the measured backscattered electric field from the ground target incident on the receiving antenna E_e^g (V m^{-1}) by

$$I_N = \frac{1}{2} c \epsilon_0 \frac{1}{N} \sum_{n=1}^{N} (E_e^g(f_n) - \langle E_{cr}^g \rangle - E_b)^2 \tag{C5}$$

C2   Fading and bandwidth selection

Fading is the phenomena that radar return of a distributed target with uniform electromagnetic properties has varying magnitudes and phases when different locations or slightly different frequencies are measured (?), (?). To remove this varying nature from a surface-classifying quantity like σ_{pq}^0 averaging must be performed. By definition σ_{pq}^0 is the average radar cross section of a certain type of distributed target, e.g. forest, asphalt, wheat field, normalized by the illuminated physical surface area. σ^0 is proportional to the average measured received power P^{Rx} (Eq. 3) or intensity $\bar{I}$. Therefore, determining $\bar{I}$ and σ^0 requires N statistically independent samples so that the sample average I_N approaches the actual average $\bar{I}$ proportionally to $1/\sqrt{N}$ in

accordance with the central limit theorem.

Practically, this can be done either by measuring I at N different locations over the surface, called spatial averaging, or with the frequency averaging -technique (see for example (?)). With the latter, physical properties governing the scattering, permittivity and surface roughness are considered frequency invariant over a certain bandwidth. Subsequently, N different frequencies should be selected according to some criteria that accounting for fading. Both averaging techniques can be used simultaneously as done by ? to increase the total number of independent samples. We solely applied the frequency-averaging technique because during the time-series measurements our antennas were in a fixed position and orientation. We assumed the single footprint area to be representative for the whole surface of the Maqu site. In Sec. 6.3 we show this assumption is justified. The used method for finding the number N of statistically independent samples within a bandwidth BW is described in ?:

$$N = \frac{2BW\Delta R}{c} \tag{C6}$$

where $\Delta R = r_{sg} - r_{eg}$. Subsequently, with $N-1$ intervals of Δf (Hz), N frequencies are selected from within BW.

As indicated above, with the application of the frequency averaging technique it is assumed that the backscatter behaviour across the selected BW is uniform. To assess the validity of this assumption for bare surface, the improved integral equation method (I^2EM) surface scattering model (?) is applied using the roughness parametrization reported in ? and a (frequency dependent) effective dielectric constant $\epsilon_{soil}(f)$ according to the dielectric mixing model by ?.

Over a BW the mean value $\langle \sigma^0(BW) \rangle$ is calculated, followed by the ratios $\sigma^0(BW_{lo})/\langle \sigma^0(BW) \rangle$ and $\sigma^0(BW_{hi})/\langle \sigma^0(BW) \rangle$ to quantify the change of σ^0 over the BW. In general the I^2EM model predicts that the change is largest for long- and smallest for short wavelengths and that it is largest for hh polarization and smallest for vv polarization. Furthermore, the RMS surface height is the most sensitive target parameter. As an example, figure C1 shows the calculation result for hh polarization with a BW of 0.5 GHz. From the graph we can read that for a centre frequency of 2.75 GHz that the retrieved σ^0_{hh} for that BW can be expected to vary $+1.0$ to -1.2 dB for $\theta = 50°$.

Based on the above calculations we chose $BW = 0.25$ GHz for L-band, $BW = 0.5$ GHz for S- & C-band, and $BW = 1.0$ GHz for X-band. These bandwidths will lead to N-values around 10 which is sufficient to let the probability density function of I_N approach a Gaussian distribution, as explained in Sec. 3.0.1. Further increment of BW was considered not to outweigh the loss of frequency resolution, especially at S-band.
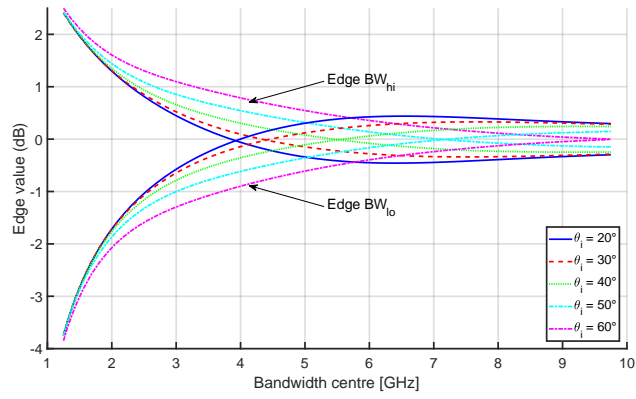
Figure C1. ~~Beamwidths~~ Variation of ~~dual polarization antennas~~σ_{hh}^0 per BW calculated with combined I^{2}EM- (**?**) and Dobson (**?**) model. ~~Shown is~~ Horizontal axis shows centre frequency of bandwidth $BW = 0.5$ GHz. Curves indicate the ~~full width half max~~ values (~~FWHM~~in dB) to be added to $\langle\sigma_{hh}^0(BW)\rangle$ at edges of ~~the measured radiation intensity patterns in the two principal planes (?)~~BW for different θ angles. Shown calculation uses: $s = 1$ cm, $\ell = 10$ cm, $m_v = 0.25$ m^3 m^{-3}, and $T_{soil} = 15\,^\circ$C.
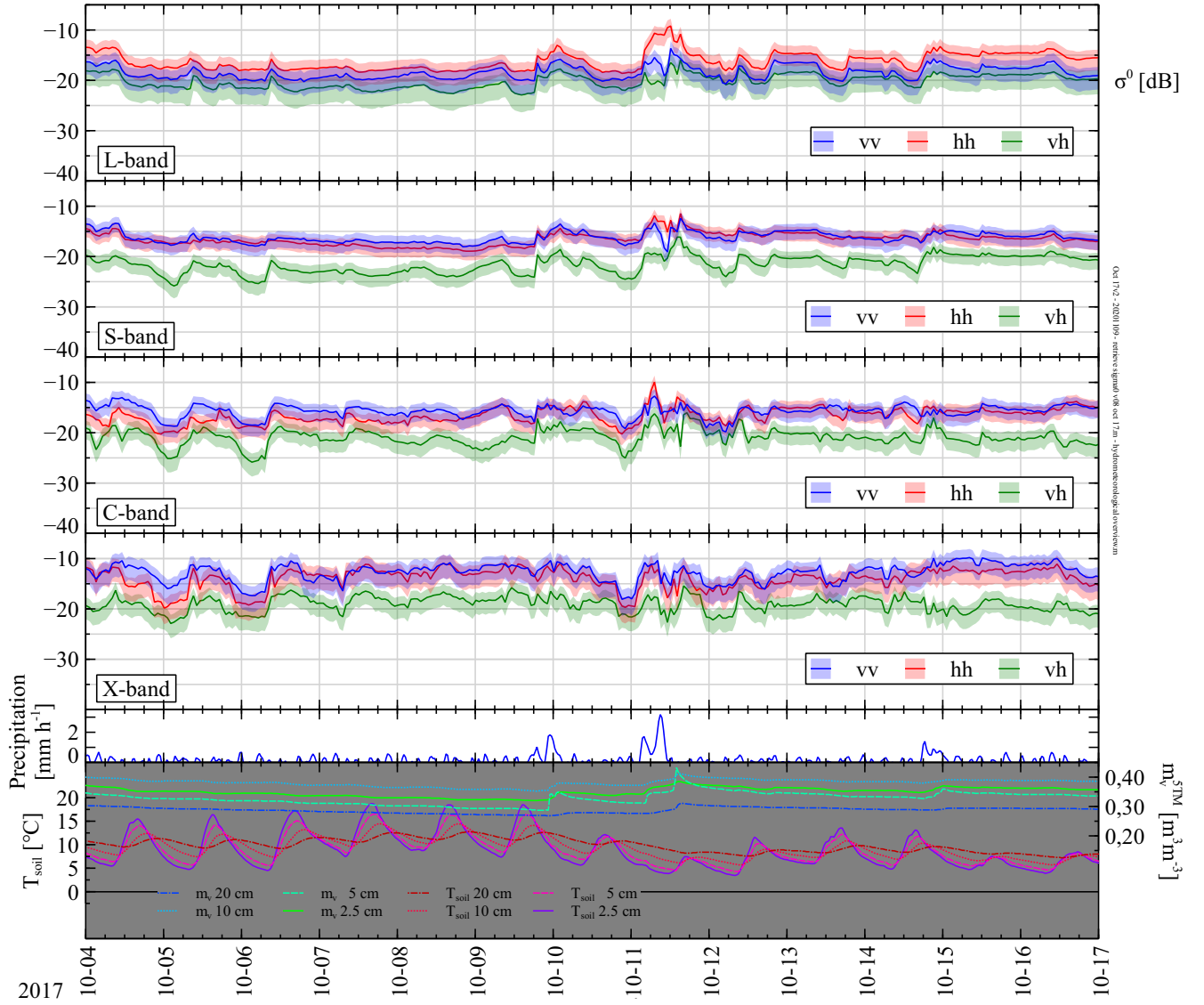
Figure D1. Time-series measurements of σ^0_{pq} (m^2 m^{-2}) for L-, S-, C- and X-band, precipitation, M_v and T_{soil} during 13 days in October 2017. Shaded regions indicate 66% confidence intervals for σ^0_{pq}. Antenna boresight angle fixed at $\alpha_0 = 55°$. The incidence angle ranges are band- and polarization dependent. Widest ranges are: L-band: $0° \leq \theta \leq 60°$, S-band: $20° \leq \theta \leq 60°$, C-band: $36° \leq \theta \leq 60°$, and X-band: $47° \leq \theta \leq 59°$. Bottom graphs show measured precipitation (mm hr^{-1}), volumetric soil moisture m_v^{5TM} (m^3 m^{-3}), and soil temperature T_{soil} at indicated depths. Spatial average volumetric soil moisture content M_v is estimated as $M_v = m_v^{5TM} \pm 0.04$ m^3 m^{-3}.
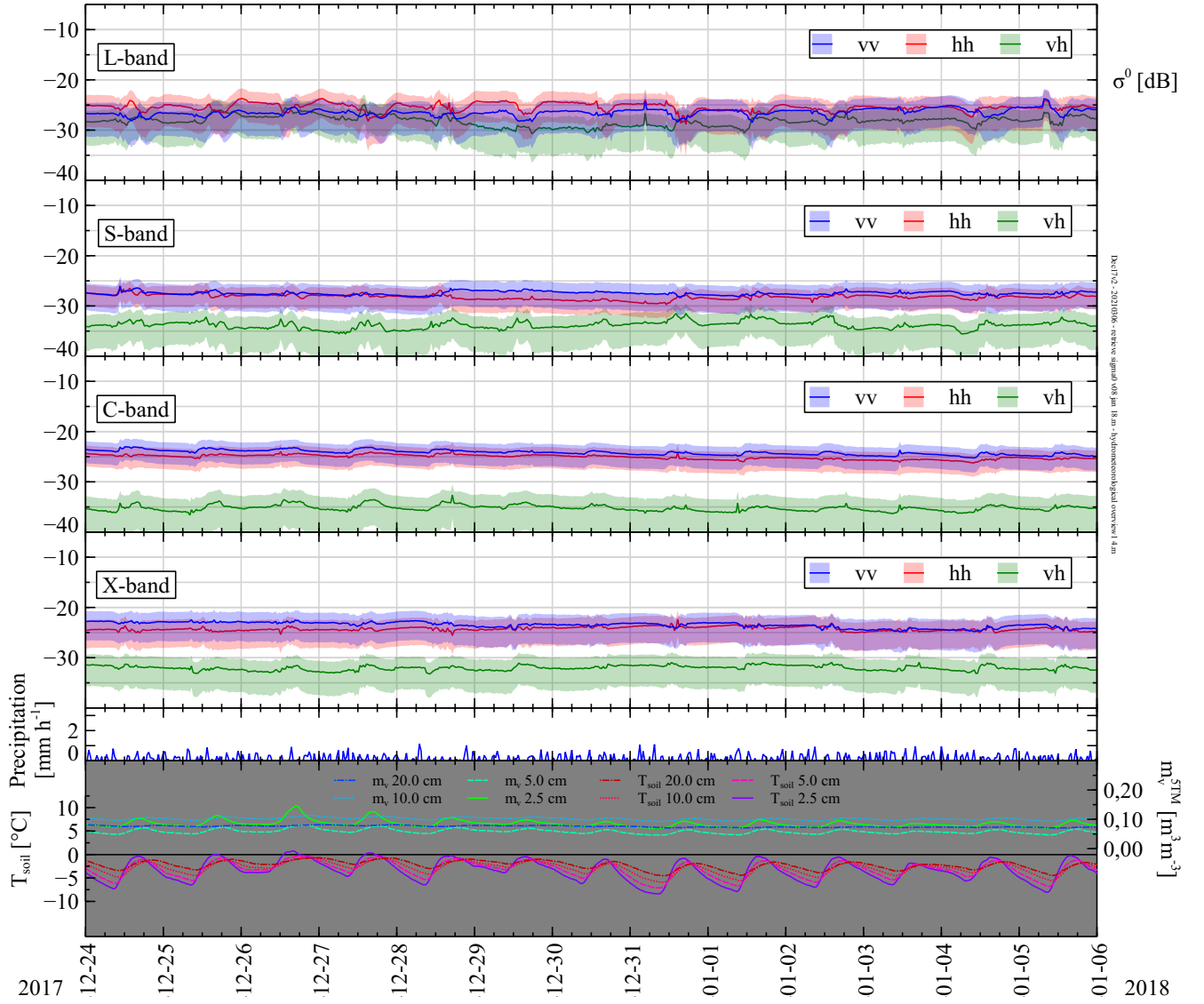
Figure D2. Time-series measurements of σ_{pq}^0 ($\mathrm{m}^2\,\mathrm{m}^{-2}$) for L-, S-, C- and X-band, precipitation, M_v and T_{soil} during 13 days in December 2017. Same configurations as Fig. D1 apply.
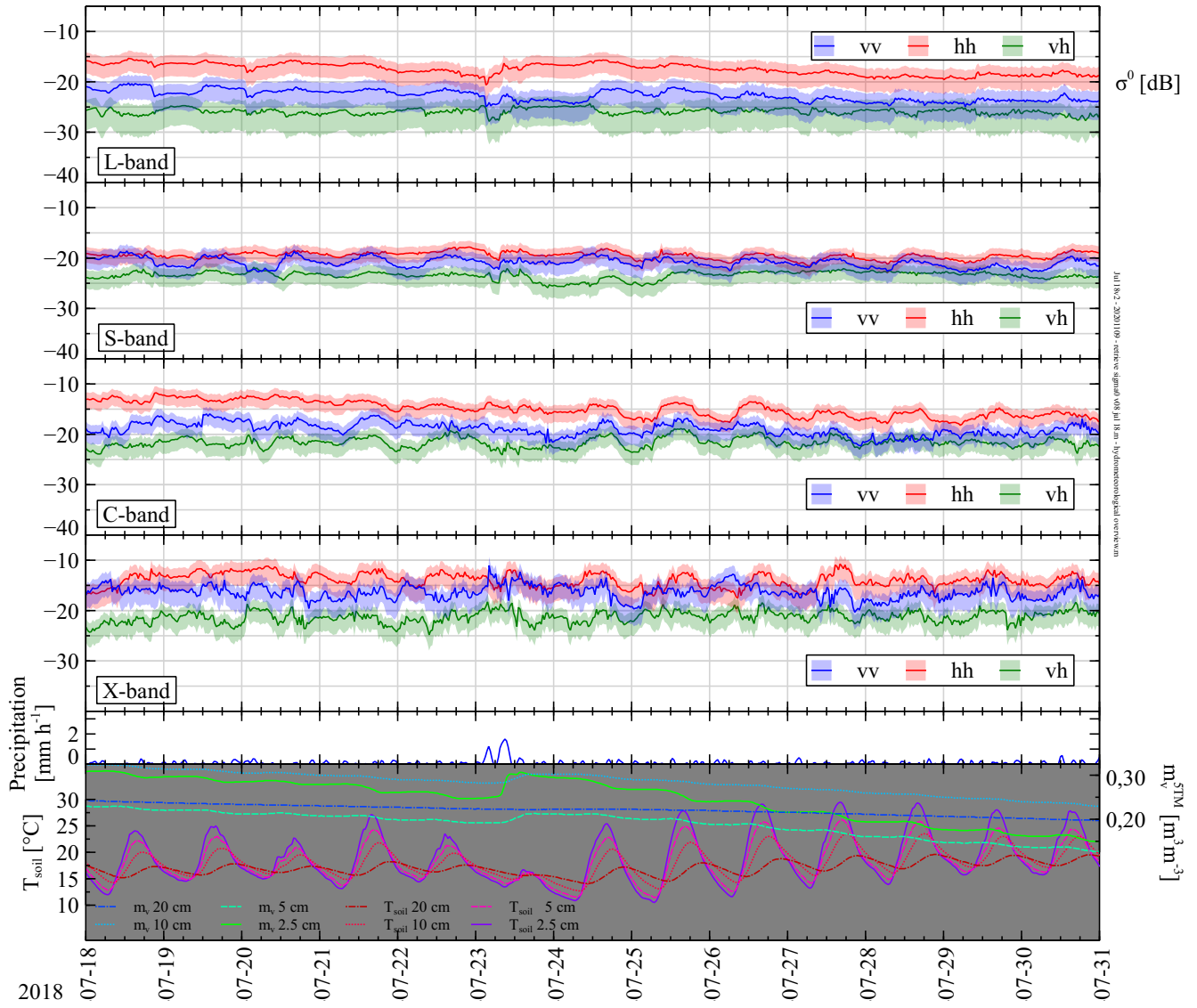
Figure D3. Time-series measurements of σ_{pq}^0 ($m^2\,m^{-2}$) for L-, S-, C- and X-band, precipitation, M_v and T_{soil} during 13 days in July 2018. Same configurations as Fig. D1 apply.

Appendix E: Details on sources of measurement uncertainty

E1 Overview measurement uncertainty

Table E1 lists all systematic measurement uncertainties and -offsets per BW and polarization channel. The uncertainty ΔK (Appendix E3) and σ_{min} values are shown as is, but for the other quantities the resulting receiver power levels (in dBm) are shown to allow for comparison with other systems. As explained in Appendix B1 the VNA actually measures the four S-parameters, which are the (complex) ratios of the received- over the transmitted wave voltage for the four polarization channels. The received wave voltages are proportional to the different electric field strengths E_e, E_0, etc. described in Sec. 3.0.1. The transmitted wave voltage, or actually its power, is constant at 10 dBm with all measurements. For the calculation of σ^0 by Eq. C1 it is irrelevant whether the electric field strengths, wave amplitudes or S-parameter magnitudes are used since the transmission-related components and/or prefactors simply cancel out. Conversion from measured S-parameters (which are associated with the corresponding scattered electric field strengths) to receiver power is done by subtracting -16 dB, which was added by the VNA software to account for the test-port coupler, and adding 10 dBm. As an example we consider a ground measurement taken on 2017-12-24 00:10:00. The VNA measured $dB(S_{11}) = -85.24$ dB for 2.8 GHz (S-band) with vv polarization. The power at the VNA receiver then was $-85.24 - 16 + 10 = -91.24$ dBm.

From Table E1 we observe that the received power associated with ΔE_T (Appendix E2) and E_{cr}^g (Appendix E4) are, in general, highest for L- and lowest for X-band. Also, the cross polarization channels have lower values than those for co polarization. As for ΔE_T, we do not have a clear explanation for this behaviour. For $\langle E_{cr}^g \rangle$ we argue that the L-band values are highest due to the stronger coupling because of the broadest radiation patterns at that band. The co- values are higher than with cross polarization because of how the electric-field lines allow for better coupling with the former. The power levels associated with E_b were derived from the specifications documentation of the VNA (?). The 'typical' receiver noise levels described therein are specified for a 10 Hz IF bandwidth. Since we measured with a broader 1 KHz IF bandwidth we added 20 dB to obtain the values in Table E1. We like to mention here that the values associated with $\langle E_{cr}^g \rangle$ for X-band and the hv channel of C-band were actually lower than the -120 dBm levels associated with E_b. We do not have a clear explanation for this. We therefore consider the E_b as the absolute minimum signal levels and therefore adjusted the values to this level.

The variation of σ_{min} over the bands and polarization channels is due to the variation in measured values of E_0^{g0}. Overall the minimum RCS is about -50 m^2 (dB). Other studies use the more appropriate so-called noise-equivalent σ^0 (m^2 m^{-2}) to quantify the minimum detectable (distributed) target, see for example ? or ?. Because of our broad antenna radiation patterns, however, this quantity is not suitable and therefore we instead refer to a discrete target extending a small solid angle.

Table E1. Summary of systematic uncertainties, -offsets and minimum signal levels. Concerning ΔE_T, E_{cr}^g, and E_b: table values are receiver power levels derived from measured S-parameters which, in their turn, are associated with ΔE_T, E_{cr}^g, and E_b. With ΔK and σ_{min} actual values are shown.

		L-band	S-band	C-band	X-band
Uncertainties					
Temperature-induced radar return uncertainty ΔE_T.	vv	-95	-98	-95	-103
$dB(\Delta S_T) - 16\text{ dB} + 10\text{ dBm} = (\text{in dBm}) \rightarrow$	vh	-107	-103	-103	-104
where ΔS_T is measured S-parameter associated	hv	-103	-104	-104	-103
with ΔE_T.	hh	-98	-92	-96	-103
Reference target measurement uncertainty ΔK.	vv	± 0.1	± 0.1	± 0.2	± 1.0
Relative error (in dB) $\rightarrow$	vh	± 0.4	± 0.1	± 0.2	± 0.8
	hv	± 0.4	± 0.1	± 0.2	± 0.8
	hh	± 0.1	± 0.1	± 0.3	± 1.0
Offsets and minimum signal levels					
Offset due to antenna coupling remnant E_{rc}^g.	vv	-86	-103	-113	-120
$dB(\langle S_{cr}^g \rangle) - 16\text{ dB} + 10\text{ dBm} = (\text{in dBm}) \rightarrow$	vh	-92	-102	-119	-120
where $\langle S_{cr}^g \rangle$ is measured S-parameter, averaged	hv	-96	-104	-120	-120
over BW, associated with E_{cr}^g.	hh	-82	-91	-107	-120
Minimum detectable signal level E_b.					
$dB(S_b) - 16\text{ dB} + 10\text{ dBm} = (\text{in dBm}) \rightarrow$		-119	-120	-120	-120
where S_b is measured S-parameter, averaged					
over BW, associated with E_b.					
Minimum detectable RCS value σ_{min}.	vv	-53	-52	-51	-48
Given target distance is R_{fp} (m^2 expressed in dB) $\rightarrow$	vh	-49	-51	-51	-49
	hv	-50	-52	-51	-51
	hh	-53	-54	-52	-50

This is the new version of old table 4

E2 Temperature-induced radar return uncertainty

The performance of the VNA's transmitters and receivers will vary due to variations of their operational temperatures, which in our case are directly linked to the temperature inside the VNA enclosure $T_{encl.}$. Many scatterometer systems employ a so-called internal calibration loop, see for example **?**, **?**, and **?**. This means that besides, or in between, scatterometer measure-
ments the transmitter and receiver are connected, via a switch, ~~trough~~ through a reference transmission line of fixed length that has a pre-determined attenuation and phase. This way, any fluctuations in the transmitter and/or receiver output over time can be measured and consequentiality removed from the target response. Instead of such an internal calibration loop we employ a different method to account for temperature-induced fluctuations of the VNA's transmitter and receiver performance.

During a half-day timespan the antennas were aimed at a fixed target at 21 m distance: the bare metal mast (without the pyramidal absorbers in front) with on top a metal sphere. At half-hour intervals the radar return was measured together with $T_{encl.}$. The fixed target was assumed to remain constant during that time, so any changes in the radar return were attributed to the changing $T_{encl.}$, which varied from $25 - 35\ ^{\circ}$C during the experiment.

For bandwidths at L-band ($1.50 - 1.75$ GHz), S-band ($2.5 - 3.0$ GHz), C-band ($4.5 - 5.0$ GHz), and X-band ($9.0 - 9.9$ GHz) the radar returns E_f (V m^{-1}) (subscript f for 'fixed target') were filtered by a gate placed over the fixed target time-domain response, resulting in E_f^{gf} (superscript gf for 'gate over fixed target'). The change of E_f^{gf} over time t, and thus over $T_{encl.}$, is denoted $\Delta E_f^{gf}(T_{encl.})$:

$$\Delta E_f^{gf}(T_{encl.}) = E_f^{gf}(t) - E_f^{gf}(t=0) \tag{E1}$$

In Fig. E1 the ~~bandwidth-average results of $\Delta E_f^{gf}(T_{encl.})$ are shown~~ over time results of this experiment are shown. Plotted are the bandwidth-average difference of the S-parameter magnitudes over time (and temperature) with respect to the reference value $\Delta S_f^{gf}(T_{encl.})$, alongside with $T_{encl.}$. As explained in the main text, the quantities actually measured by the VNA were the S-parameters, which are proportional to the corresponding values E_f^{gf} and $\Delta E_f^{gf}(T_{encl.})$.

There appeared to be no unique relationship between ~~ΔE_f^{gf}~~ ΔS_f^{gf} and $T_{encl.}$. Within three hours from the experiment start $T_{encl.}$ increases to a maximum value after which it decreases again at an increasingly slowed rate. Also the curves ~~$\Delta E_f^{gf}(T_{encl.})$~~ $\Delta S_f^{gf}(T_{encl.})$, in general, change more rapidly over the first five hours and then become more stable. However, the direction of change in $T_{encl.}$: a rapid increase at the start, followed by a decrease after 19:15 at an increasingly slow rate is not seen in the ~~$\Delta E_f^{gf}(T_{encl.})$~~ $\Delta S_f^{gf}(T_{encl.})$ curves. So in order to quantify the temperature-induced VNA instability we used the maximum observed variation of ~~$\Delta E_f^{gf}(T_{encl.})$~~ $\Delta S_f^{gf}(T_{encl.})$ over time amidst all frequencies within ~~the considered~~ BW to calculate the temperature-induced radar return uncertainty ~~ΔE_T^g () as~~ ΔS_T. Or, in the context of scattered electric field strengths, its corresponding value ΔE_T (V m^{-1})

$$\Delta E_T^g = \frac{max[\Delta E_f^{gf}(T_{encl.})] - min[\Delta E_f^{gf}(T_{encl.})]}{2} \tag{E2}$$

Figure E1. Measured radar return from a fixed target over a varying enclosure temperature $T_{encl.}$

~~Table E1 lists ΔE_T^g values for the considered bandwidths and polarizations. ΔE_T^g~~ The quantity ΔE_T is to be treated as an absolute uncertainty of E_e^g (Eq. C5) according to:

$$I_N = \frac{1}{2} c\epsilon_0 \frac{1}{N} \sum_{i=1\,n=1}^{N} (E_e^g(f_{in}) - \langle E_{ncr}{}^g (f_i)\rangle - E_b \pm 2\Delta E_{eT}^g)^2 \tag{E3}$$

1140   with a factor two since both $E_e^g(f_i)$ and $E_b^g(f_n)$ are subject to this temperature-induced uncertainty. Table E1 lists the power levels at the VNA's receivers calculated from ΔS_T for the considered bandwidths and polarization channels.

E3   Reference target measurement uncertainty

E3.1   Reference target alignment

The absolute backscattering coefficient is determined with respect to the known RCS of a reference target. Errors in the used

1145   reference target's RCS itself, or errors made during the measurement of that target will contribute to the ~~σ_0~~ σ^0 uncertainty. The RCS of a rectangular metal plate calculated with Eq. (B2) was found to match experimental observations fairly well (**?**), and therefore errors in the RCS of our rectangular plate itself were not considered. For the dihedral reflector we do the same, keeping in mind that only the specular component was selected in time domain, thereby omitting interference from diffraction of the dihedral's edges. Should the gate have been wide enough to also cover these diffraction Eq. B2 will not be suitable

anymore, see for example (?). We did consider errors in the measurement of the reference target, specifically we considered misalignment of the scatterometer's antennas towards the rectangular plate and vice versa.

The angular position of the reference targets with respect to the antenna boresight direction was estimated to be $-2.25° \leq \beta_0 \leq 1.25°$ in the horizontal direction and $-1.3° \leq \alpha_0 \leq 1.3°$ in the vertical direction. Given the large distance from the antennas to the rectangular plate, $R_0 = 36.3$ m, and the much smaller separation between the transmit- and receive antennas, $W_{ant} = 0.4$ m, single uncertainty values $\Delta\alpha_0$, $\Delta\beta_0$ were used for both antennas. Due to this possible antenna misalignment the reference target is not illuminated by the peak value of the gain pattern, i.e. $G = G(\alpha_0 \pm \Delta\alpha_0, \beta_0 \pm \Delta\beta_0)$ (−), resulting in an uncertainty in the measured radar response of the reference target, and thus in K (W m^{-1}). Equation C3 then is modified to

$$K = \frac{1}{2}c\epsilon_0\left(E_b^{gcg0} - E_b\right)^2 \frac{G(\alpha,\beta)^2}{G(\alpha_0 \pm \Delta\alpha_0, \beta_0 \pm \Delta\beta_0)^2}\left(\frac{R_0}{R_{fp}}\right)^4 \frac{A_{fp}}{\sigma^{bi}(\theta_i \pm \Delta\theta_i, \phi_i, \theta_s \pm \Delta\theta_s, \phi_s)} \tag{E4}$$

The angular position of the individual antennas with respect to the reference target's surface normal (or frontal projection surface normal in case of the dihedral reflectors) was estimated with the help of a laser mounted between the two antennas and detachable mirrors on the reference targets. Optimal alignment was found by rotating the targets until the reflected laser spot was on (or close to) the laser aperture again. In the horizontal plane, the angle between the rectangular plate's surface normal and the transmit antenna was $\theta_i = 0.16°$ (right side of the normal) and for the receive antenna $\theta_s = -0.48°$. In the vertical plane, the angle between the rectangular plate's surface normal and both antennas (as they are next to each other) was close to zero. We estimated the uncertainty of all aforementioned angles to be $\Delta\theta_i = \Delta\theta_s = 0.10°$ (both in the horizontal- and vertical plane.) For the small dihedral reflector these angles were $\theta_i = \theta_s = 0 \pm 0.2°$ in horizontal- and vertical plane while for the large dihedral reflector $\theta_i = 1.34 \pm 0.2°$ & $\theta_s = 0.52 \pm 0.2°$ in horizontal- and $\theta_i = \theta_s = 0.72 \pm 0.2°$ in vertical plane.

Starting with the physical optics model for the monostatic RCS of a metal rectangular plate, $\sigma(\theta,\phi)$ (?) p. 457, a crude bistatic-RCS version $\sigma^{bi}(\theta_i,\phi_i,\theta_s,\phi_s)$ was created by simply imposing a linear phase delay along the plate's surface. We shall assume that this model will also hold for the dihedral reflector. Calculation of K can then be extended to include the (mis)alignment or offset of both individual antennas with respect to the reference targets and their uncertainties, which leads to Eq. E4.

How the uncertainties $\Delta\alpha_0$, $\Delta\beta_0$, $\Delta\theta_i$, and $\Delta\theta_s$ in Eq. E4 propagate into the uncertainty of K, called the reference target measurement uncertainty ΔK, may be found in textbooks such as ?.

Resulting ΔK values, per considered BW and polarization, are presented as relative uncertainties in Table E1. With X-band the ΔK values are highest because the antenna radiation patterns are most narrow for higher frequencies.

1185

1190
E3.1 Validation reference target alignment

In this section we shall demonstrate that estimated values for the rotational offsets and uncertainties $\theta_i, \theta_s, \Delta\theta_i, \Delta\theta_s$ of used reference targets are consistent with their respective measured radar returns. First we apply the radar equation (Eq. 1) to both the rectangular plate and the small dihedral reflector and substitute for P^{Tx}. We then have

$$\sigma_{dih}^{bi}(\theta_i^{dih}, \phi_i, \theta_s^{dih}, \phi_s) = \frac{P_{dih}^{Rx}}{P_{pla}^{Rx}} \frac{G(\alpha_0 \pm \Delta\alpha_0, \beta_0 \pm \Delta\beta_0)^2}{G(\alpha_0 \pm \Delta\alpha_0, \beta_0 \pm \Delta\beta_0)^2} \left(\frac{R_{dih}}{R_{pla}}\right)^4 \sigma_{pla}^{bi}(\theta_i^{pla}, \phi_i, \theta_s^{pla}, \phi_s) \tag{E5}$$

1195
where we dropped the polarization subscripts for readability. Since the values for α_0 and β_0 are the same for both measurements the term containing the antenna gain patterns G is unity. We then end up with

$$\frac{\sigma_{dih}^{bi}(\theta_i^{dih}, \phi_i, \theta_s^{dih}, \phi_s)}{\sigma_{pla}^{bi}(\theta_i^{pla}, \phi_i, \theta_s^{pla}, \phi_s)} = \left(\frac{R_{dih}}{R_{pla}}\right)^4 \frac{P_{dih}^{Rx}}{P_{pla}^{Rx}} \tag{E6}$$
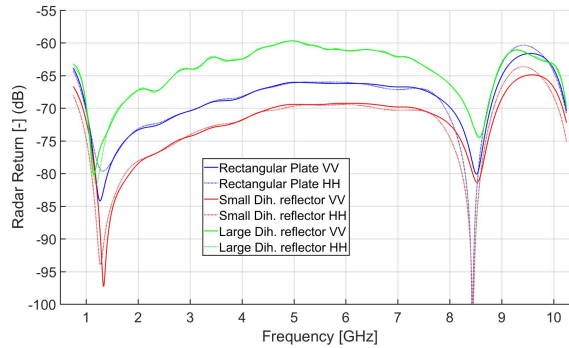
Figure E2. Measured radar returns of calibration standards for co polarization E_0^{g0}. Solid lines are VV- and dotted lines are HH polarization.

Figure E2 shows the measured radar returns of the three calibration standards. For 5 GHz the difference between the small dihedral return P_{dih}^{Rx} and the rectangular plate P_{rect}^{Rx} for vv polarization is -3.3 dB. The term involving the distances R is -4.7

1200
dB resulting in the right-side of Eq. E6 to be -8.0 dB. If both reference targets were perfectly aligned towards the antennas the

RCS ratio on the left-side of Eq. E6 is -8.1 dB, which is 0.1 dB below the measured result. By finding suitable combinations of misalignment- or offset angles θ_i, θ_s for both targets Eq. E6 can be satisfied. It can be shown that consistent angles can be found for all three reference targets which are within the ranges specified in section E3.1. In the above procedure we used the co-polarization returns of the dihedral reflectors, while it is in fact the cross-polarization that is of interest. The 45° rotation of the references for realizing the depolarization did not introduce significant other angular offsets. Note that the explained method cannot validate the angular positions of the reference targets with respect to the antenna boresight direction and their uncertainties: α_0 & $\Delta\alpha_0$ and β_0, $\Delta\beta_0$ as the term containing the antenna gain patterns was cancelled out.

We conclude this section with some remarks on the features in the measured reference target return powers shown in Fig. E2. With all returns there is a sharp trough between $8 - 9$ GHz, which is caused by a combination of a local increment of the antenna's return loss and an asymmetry in the antennas E-plane radiation pattern between $7 - 9$ GHz. The asymmetry causes the pattern's peaks to point off-target by about 10° resulting in a lower radar return. The deep troughs close to 1.3 GHz are caused by a combination of high return loss at the low-frequency edge of the antenna's operational bandwidth and an artefact of the gating procedure, which in this case lets $E_0^{g0}(f)$ rise at the edge. This gating artefact is known to distort the band edges of a gated frequency response (?). To account for this artefact the bandwidths used for the ground surface measurements were broadened by 10% at both edges prior to gating. The added edges were discarded again after gating. The curves of the rectangular plate and small dihedral reflector have a similar shape for most of the frequency band. Their difference is merely a constant factor as predicted by the physical optics model for RCS (Eq. B2). The curve shape of the large dihedral reflector however is clearly different from the other two. This is partly because of its more severe angular offsets θ_i and θ_s but also because the planar-wave condition is not met for most of the frequency band, see Table B1.

E4   Antenna coupling remnant

Because the transmit- and receive antennas are placed next to each other in order to measure the monostatic σ^0 that can be measured given E_n^g and part of the transmitted signal leaks, or couples, directly into the receive antenna, thereby interfering with the target return of interest. This antenna coupling is strongest for the lower frequencies (L-band) because these have the broadest antenna radiation patterns (see Fig. B3). With respect to the polarization channels, the antenna coupling is strongest for hh because of how the electric field lines of the principal TE_{10} modes, in the particular case of hh polarization, couple strongest when the antenna apertures are next to each other. With the cross polarization channels the coupling is weakest because of how the principal field components are perpendicular between the transmit- and receive antenna.

Although the majority of the antenna coupling can be filtered out by gating, a remnant remains present in the filtered frequency domain response. This becomes apparent when the antennas are pointed skywards and the other scatterometer's parameters such as R_{fp} () time-domain response is calculated per BW. Between the times/distances $r_{sg} = ct_{sg}/2$ and A_{fp} (). The NES is calculated by assuming E_n^g as the radar return in Eq. C1.Table E1 summarizes the noise-floor levels and subsequent NES values per considered bandwidth and polarization. The higher NES level for S-band $r_{eg} = ct_{eg}/2$ where, during measurement

of the ground target, the scattering events of interest are located the signal is not yet at its lowest level beyond 10 m. This effect is strongest for the L-band BW with hh polarization ~~is attributed to a stronger interaction of the antenna's near-field radiation pattern with the tower features.~~ while for X-band the time-domain response level between r_{sg} and r_{eg} is almost equal to its lowest level.

From the sky measurement the coupling remnant $E_{cr}^g(BW)$ was retrieved. When measuring the ground surface, the antenna coupling process of course interferes with the ground return. However, because we measure over a bandwidth and the ground return is a randomly fluctuating signal we argue that $\langle E_{cr}^g(BW) \rangle$, so the average over BW, can simply be subtracted from the (gated) ground return $E_e^g(BW)$.

E5 Propagataion of uncertainties

In this section we demonstrate how Eq. 4 is derived. We show, using error-propagation theory, how each of the (three) error-terms ~~ΔE_T^g~~ ΔE_T, ΔK, and fading, propagates into an error for σ^0 and how all errors may be combined into one statistical confidence interval for σ^0. We start with Eq. C1, which with Eq. C4 can be written as

$$\sigma^0 = \frac{\bar{I}}{K} = \frac{I_N}{K(1 \pm 1/\sqrt{N})} \tag{E7}$$

The term between brackets in the denominator we may simply rewrite as $F \pm \Delta F$, i.e. a variable with an error. The variables I_N and K also have their respective errors ΔI_N and ΔK. When we write all variables and their errors explicitly we end up with

$$\sigma^0 = \frac{I_N}{KF} = \frac{I_N \pm \Delta I_N}{(K \pm \Delta K)(F \pm \Delta F)} \tag{E8}$$

We shall now describe all three error terms, starting with ΔI_N. The calculation of I_N from the measured backscattered electric field is given by Eq. E3 as

$$I_N = \frac{1}{2} c \epsilon_0 \frac{1}{N} \sum\nolimits_{i=1 \, n=1}^{N} (E_e^g(f_{in}) - \langle E_{ncr}{}^g(f_i) \rangle - E_b \pm 2\Delta E_T{}^g)^2 \tag{E9}$$

with ~~ΔE_T^g~~ ΔE_T as measurement uncertainty. As explained in Sec. C2, every term in the above sum may be considered an independent variable. Because the number of samples N within BW is sufficiently large (about 15) we consider ~~ΔE_e^T~~ ΔE_T as a statistical error and therefore use the corresponding equation for error propagation (see for example **?**) to calculate the total statistical error ΔI_N:

$$\Delta I_N = \frac{1}{2} c \epsilon_0 \frac{2\Delta E_T^g}{N} \sqrt{\sum_{i=1}^{N} (E_e^g(f_i) - E_n^g(f_i))^2} \frac{4\Delta E_T}{N} \sqrt{\sum_{n=1}^{N} (E_e^g(f_n) - \langle E_{cr}^g \rangle - E_b)^2} \tag{E10}$$

ΔI_N can be considered as the one-standard-deviation value of I_N. Since the number of terms in the sum N are large enough we can consider $\pm \Delta I_N$ as the edges of a 66 % confidence interval for I_N.

As explained in Sec. ~~??~~ E3.1, ΔK can be calculated by using error propagation theory for the errors $\Delta\alpha_0$, $\Delta\beta_0$ and those associated with the bistatic RCS of the rectangular metal plate and dihedral reflectors $\Delta\theta_i$ and $\Delta\theta_s$. Note however that ~~$\Delta\alpha_0$ and $\Delta\beta_0$~~ these are maximum possible errors so ~~the appropriate~~ that the corresponding error propagation rules should be used. In order to have differentiable functions for the E-plane and H-plane antenna gain patterns, $E_{patt}(\alpha_0)$ and $H_{patt}(\beta_0)$ respectively, the measured radiation patterns can be fitted with Gaussian functions for angles close to antenna boresight. Writing ΔK explicitly is then straightforward.

Finally the error ΔF, which of course is $1/\sqrt{N}$. As explained in Sec. C1 this error represents a 68% confidence interval for $\bar{I}$.

Returning to Eq. E8 we now combine all three errors into one statistical error. To do so we must first convert ΔK from being a maximum possible error into a statistical error like ΔI_N and ΔF. This can be done by multiplying ΔK with 2/3, so the result may be interpreted as a one standard deviation value for K. This is equivalent to saying that $\pm 2/3\Delta K$ is a 68 % confidence interval for K. We combine the three statistical errors conservatively into a 66 % confidence interval for σ^0:

$$\sigma^0 = \frac{I_N}{KF} = \frac{I_N \pm \Delta I_N}{(K \pm \frac{2}{3}\Delta K)(1 \pm 1/\sqrt{N})} = \frac{I_N}{KF} \pm \Delta\sigma^0 = \frac{I_N}{K} \pm \Delta\sigma^0 \tag{E11}$$

where ~~Δ^0~~ $\Delta\sigma^0$ is calculated according to the error propagation equation for statistical errors:

$$\left(\Delta\sigma^0\right)^2 = \left(\frac{\partial\sigma^0}{\partial I_N}\right)^2 (\Delta I_N)^2 + \left(\frac{\partial\sigma^0}{\partial K}\right)^2 (\Delta K)^2 + \left(\frac{\partial\sigma^0}{\partial F}\right)^2 (\Delta F)^2. \tag{E12}$$

Table E1. Summary of systematic uncertainties, -offsets and minimum signal levels. Concerning ΔE_T, E^g_{cr}, and E_b: table values are receiver power levels derived from measured S-parameters which, in their turn, are associated with ΔE_T, E^g_{cr}, and E_b. With ΔK and σ_{min} actual values are shown.

		L-band	S-band	C-band	X-band
Uncertainties					
Temperature-induced radar return uncertainty ΔE_T:	vv	-95	-98	-95	-103
$dB(\Delta S_T) - 16$ dB $+10$ dBm $=$ (in dBm) $\rightarrow$	vh	-107	-103	-103	-104
where ΔS_T is measured S-parameter associated	hv	-103	-104	-104	-103
with ΔE_T.	hh	-98	-92	-96	-103
Reference target measurement uncertainty ΔK:	vv	± 0.1	± 0.1	± 0.2	± 1.0
Relative error (in dB) $\rightarrow$	vh	± 0.4	± 0.1	± 0.2	± 0.8
	hv	± 0.4	± 0.1	± 0.2	± 0.8
	hh	± 0.1	± 0.1	± 0.3	± 1.0
Offsets and minimum signal levels					
Offset due to antenna coupling remnant E^g_{cr}:	vv	-86	-103	-113	-120
$dB(\langle S^g_{cr}\rangle) - 16$ dB $+10$ dBm $=$ (in dBm) $\rightarrow$	vh	-92	-102	-119	-120
where $\langle S^g_{cr}\rangle$ is measured S-parameter, averaged	hv	-96	-104	-120	-120
over BW, associated with E^g_{cr}.	hh	-82	- 91	-107	-120
Minimum detectable signal level E_b:					
$dB(S_b) - 16$ dB $+10$ dBm $=$ (in dBm) $\rightarrow$		-119	-120	-120	-120
where S_b is measured S-parameter, averaged					
over BW, associated with E_b.					
Minimum detectable RCS value σ_{min}:	vv	-53	-52	-51	-48
Given target distance is R_t, (m^2 expressed in dB) $\rightarrow$	vh	-49	-51	-51	-49

Appendix F: Angular variation of σ_{pp}^0 for asphalt

We start with the asphalt experiment results, which we present here to demonstrate that our σ^0 retrieval method, using measurement data obtained with our scatterometer system, results in σ^0 values comparable to those in other studies.

Figure F1 shows our retrieved σ_{pq}^0 over α_0 for all bandwidths and polarization channels. Since with all bands the uncertainty intervals for vh and hv overlap we only show vh cross polarization channel for figure clarity. When comparing the results for S-, C-, and X-band we observe an increase in backscatter over frequency, which can be explained by the increment of the surface roughness to wavelength ratio. For X-, and C-band the vv backscatter is stronger than with hh. For S-band this also holds, although the comparison is more difficult as the θ intervals become broader. It is clear however, that for all bands the cross- response is lower than that of the co polarization. Remarkable, at first sight, is that the retrieved σ^0 for L-band is higher than that of S-band. We believe this is due to the lowest angular resolution of our system at L-band and our subsequent σ^0 retrieval method from the measured signal. As shown in the graphs, for L-band the backscatter from near-nadir θ angles are included in the received signal for almost all α_0 angular positions. As the 'actual' $\sigma^0(\theta)$, in general, shoots upward for the smaller θ-angles towards the peak value at nadir the resulting signal, and with it, the retrieved σ^0 is high as well.

Our results are plotted together with those found in other studies. **?** also measured asphalt backscatter for S-band. His scatterometer had a more narrow beamwidth of 10°, allowing for a straightforward measurement of σ^0 over θ. He measured over $15° \leq \theta \leq 55°$. For a comparison to our results, we used his measured $\sigma^0(\theta)$ in Eq. 2 and subsequently applied our retrieval method to this simulated radar return P^{Rx}. The resulting σ^0 values are shown in F1. Three points for vv-, and two for vh polarization could be retrieved. Because no data was presented outside the $15° - 55°$-range the hh polarization response could not be simulated. In general, we consider our results to match with Baldi's satisfactory. The differences may be attributed to fading uncertainty (low number of spatial samples) and to different surface roughness values: it seems our asphalt was smoother. However, the latter argument is speculative since neither we nor Baldi measured the surface roughness.

The only other study on L-band backscatter from asphalt we could find was that by **?**. There σ^0 values are reported for smooth asphalt with an estimated surface roughness of $s = 0.3$ mm for $20° \leq \theta \leq 70°$ for vv and $10° \leq \theta \leq 70°$ for hh. Because of the broad L-band θ-ranges for our scatterometer, however, a simulation of the σ^0-retrieval, as with Baldi's data, would be incorrect.

For X-band with co-polarization we compare our results with the empirical model for asphalt described in **?**. This model is formed using measurements from multiple other studies with asphalt having various roughness values. Since our antenna beamwidths at X-band are sufficiently narrow we can compare our results without further adjustment. No empirical model is given for asphalt at X-band with cross polarization in **?**. For both vv- and hh polarization our retrieved σ^0 shows a clear overall decreasing trend over θ, which is expected for a surface that is smooth compared to the wavelength. Overall, σ^0 for vv polarization is higher than for hh polarization, which is in accordance to the empirical model. Starting from the smaller angles, the consecutive measurement points remain at similar level. With hh polarization there appears to be even a local minimum

at 40°, although the measurement uncertainty is relatively large there. Given that the empirical curves show a similar trend, though not as pronounced, the slow decay of σ_{pp}^0 over θ for $25 - 55°$ can simply be a property of asphalt. Overall we find our measurements to lie within the 90 % occurrence interval of the empirical model and therefore conclude that our results for asphalt are similar to those of **?**. We could not find studies reporting asphalt backscatter for C-band.
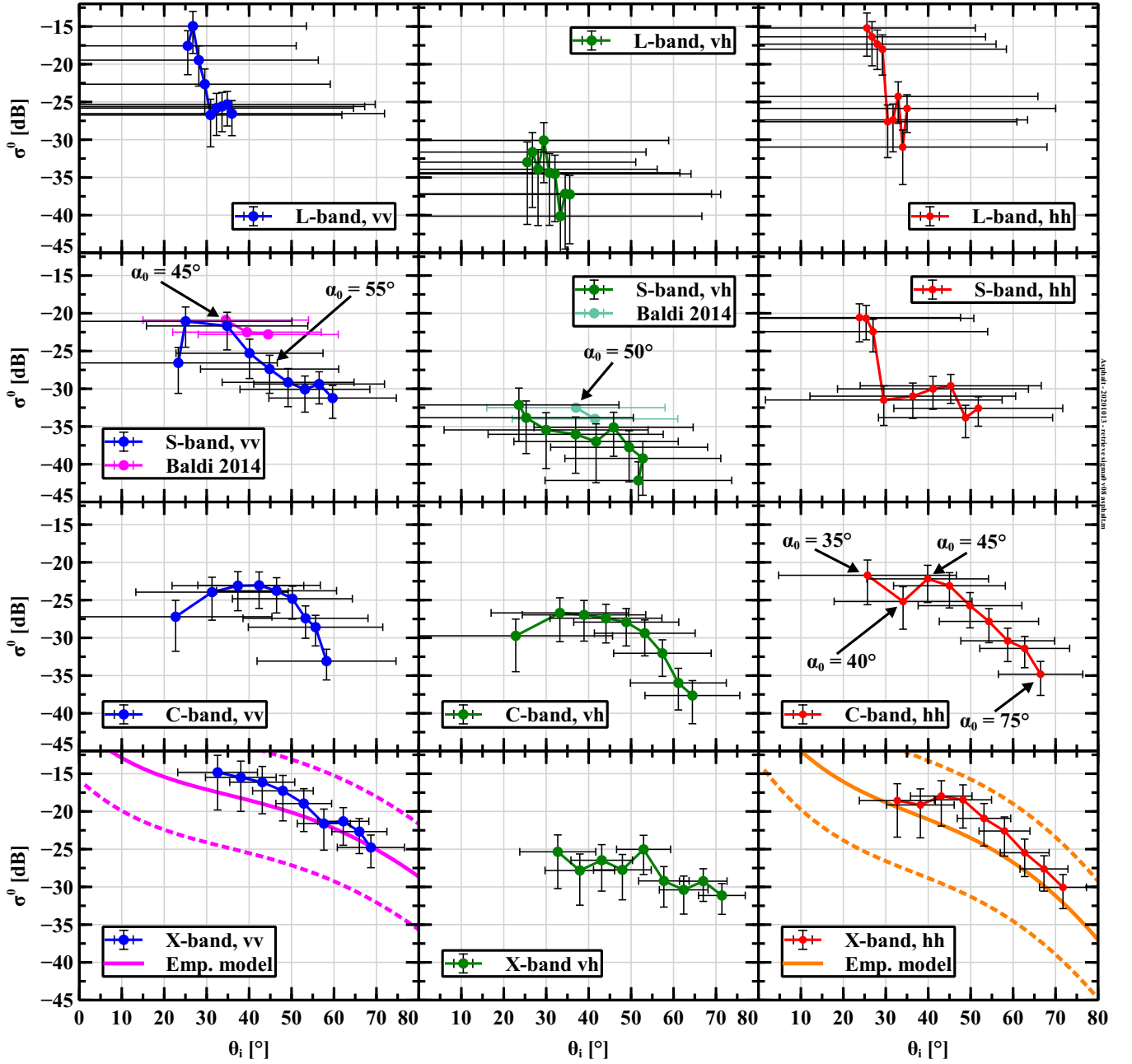
Figure F1. Measurement results of $\sigma^0_{pq}(\alpha_0)$ for all bands and polarizations together with S-band measurement results from **?** and empirical model for X-band from **?**. Points represent results for different antenna boresight angles α_0. Horizontal bars represent intervals for angle of incidence θ and vertical bars the 66% confidence interval for σ^0. Dotted lines between data points are guide to the eye. With X-band, solid and dotted curves (magenta and orange) represent mean value and 90% confidence interval of empirical model respectively.

Appendix G: Examples of σ_{pq}^0 over α_0 for Maqu
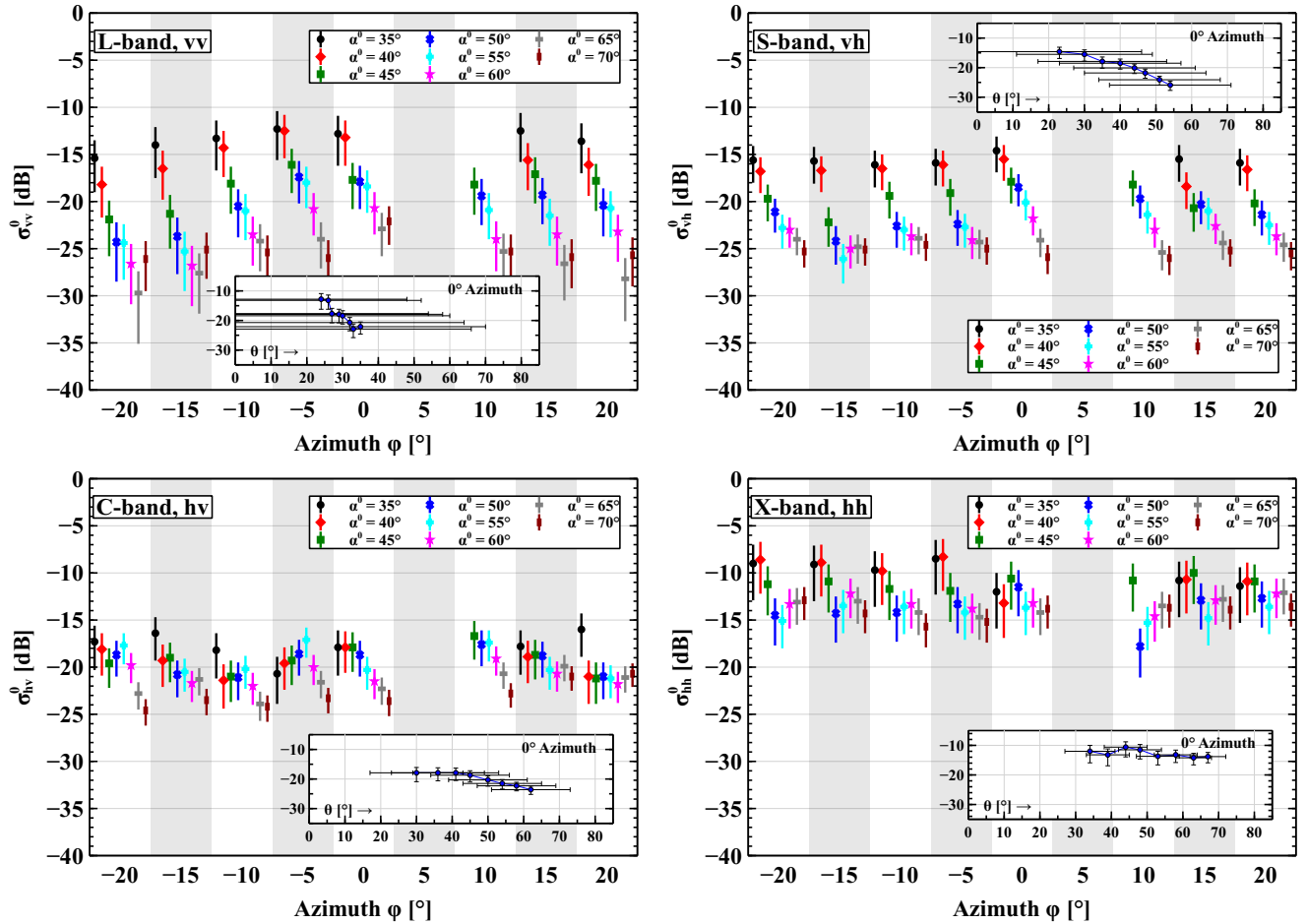
Figure G1. Measurement of $\sigma_{pq}^0(\alpha_0, \phi)$ for all bandwidths at different polarization over the Maqu site on 2017 08 25. Four main figures: For different antenna boresight azimuth angles ϕ the variation of σ_{pq}^0 over boresight elevation angles α_0 is shown. The eight vertical bars represent the 66% confidence interval for σ^0. Intervals for incidence angles θ per measurement are not shown here for clarity of figure. Insets: $\sigma_{pq}^0(\alpha_0)$ for $\phi = 0°$. Horizontal bars represent intervals of actual incidence angles θ, which are identical for other ϕ-values in main figures.

Author contributions. JH wrote this paper, installed and operated the scatterometer system, developed the data processing, σ^0 retrieval process, and performed the data analysis. RvdV advised in the experiment designs, σ^0 retrieval process and paper structure. XW, ZW and DZ, handled the China customs logistics, installed and operated the scatterometer system. On a regular basis they maintained the scatterometer system and the Maqu site. CvdT advised in the σ^0 retrieval process. JW and ZS conceptualized the experiment design. All co-authors commented and revised the paper.

1320

Competing interests. All authors declare that there are no conflicts of interests

1325   *Acknowledgements.* This work was supported in part by ESA ELBARA-II/III Loan Agreement EOP-SM/2895/TC-tc, the ESA MOST Dragon IV Program (Monitoring Water and Energy Cycles at Climate Scale in the Third Pole Environment), the Netherlands Organization for Scientific Research under Project ALW-GO/14-29, the National Natural Science Foundation of China (grant no. 41971033) and the Fundamental Research Funds for the Central Universities, CHD (grant no. 300102298307).